KeAi

CHINESE ROOTS
GLOBAL IMPACT

#### Contents lists available at ScienceDirect

# Petroleum Science

journal homepage: www.keaipublishing.com/en/journals/petroleum-science



# Original Paper

# Microscopic oil occurrence in the Permian alkaline lacustrine shales: Fengcheng formation, Mahu Sag, Junggar basin



Jia-Hao Lv <sup>a, b, c</sup>, Tao Hu <sup>d, e, \*</sup>, Wang Zhang <sup>a, b, c, \*\*</sup>, Fu-Jie Jiang <sup>d, e, \*\*\*</sup>, Jing Xue <sup>f</sup>, Chen-Xi Zhang <sup>d, e</sup>, Zhen-Guo Qi <sup>d, e</sup>, Ren-Da Huang <sup>d, e</sup>, Mei-Ling Hu <sup>d, e</sup>, Shu Jiang <sup>g</sup>

- <sup>a</sup> State Key Laboratory of Shale Oil and Gas Enrichment Mechanisms and Efficient Development, Beijing, 100101, China
- <sup>b</sup> Key Laboratory of Deep Petroleum Intelligent Exploration and Development, Institute of Geology and Geophysics, Chinese Academy of Sciences, Beijing, 100029, China
- <sup>c</sup> College of Earth and Planetary Sciences, University of Chinese Academy of Sciences, Beijing, 101408, China
- d State Key Laboratory of Petroleum Resources and Engineering, China University of Petroleum (Beijing), Beijing, 102249, China
- e College of Geosciences, China University of Petroleum (Beijing), Beijing, 102249, China
- f Research Institute of Oriental Geophysical Company, CNPC, Xi'an, 710021, Shaanxi, China
- g Key Laboratory of Tectonics and Petroleum Resources, China University of Geosciences, Ministry of Education, Wuhan, 430074, Hubei, China

#### ARTICLE INFO

# Article history: Received 15 March 2024 Received in revised form 14 July 2024 Accepted 15 January 2025 Available online 23 January 2025

Edited by Jie Hao

Keywords: Alkaline lacustrine shale Mahu sag Fengcheng formation Shale oil Occurrence mechanism

#### ABSTRACT

Alkaline lacustrine shale is highly heterogeneous, and the complex relationship between the organicinorganic porosity network and hydrocarbon occurrence restricts the effectiveness of shale oil exploration and development. Herein, we investigated the Fengcheng Formation (P<sub>1</sub>f) in Mahu Sag. This study integrated geochemistry, Soxhlet extraction, scanning electron microscopy, gas adsorption, and nuclear magnetic resonance T<sub>1</sub>-T<sub>2</sub> spectroscopy to elucidate the microscopic oil occurrence mechanisms in shales. Results indicate the presence of felsic shale, dolomitic shale, lime shale, and mixed shale within the P<sub>1</sub>f. Matrix pores and microfractures associated with inorganic minerals are the predominant pore types in P<sub>1</sub>f. Adsorbed oil primarily resides on the surfaces of organic matter and clay minerals, while free oil predominantly occupies inorganic pores and microfractures with larger pore sizes. Variations exist in the quantity and distribution of shale oil accumulation across different scales, where free oil and adsorbed oil are governed by dominant pores with diameters exceeding 10 nm and ineffective pores with diameters below 10 nm, respectively. Shale oil occurrence characteristics are influenced by organic matter, pore structure, and mineral composition. Felsic shale exhibits a high abundance of dominant pores, possesses the highest oil content, predominantly harbors free oil within these dominant pores, and demonstrates good mobility. Fluid occurrence in dolomitic shale and lime shale is intricate, with low oil content and a free oil to adsorbed oil ratio of 1:1. Mixed shale exhibits elevated clay mineral content and a scarcity of dominant pores. Moreover, ineffective pores contain increased bound water, resulting in medium oil content and limited mobility predominantly due to adsorption. Presently, shale oil mainly occurs in the dominant pores with a diameter larger than 10 nm in a free state. During the exploration and development of alkaline lacustrine shale oil resources, emphasis should be placed on identifying sweet spots within the felsic shale characterized by dominant pores.

© 2025 The Authors. Publishing services by Elsevier B.V. on behalf of KeAi Communications Co. Ltd. This is an open access article under the CC BY license (http://creativecommons.org/licenses/by/4.0/).

## 1. Introduction

The global petroleum industry is undergoing a "black shale

E-mail addresses: thu@cup.edu.cn (T. Hu), zhangwang@mail.iggcas.ac.cn (W. Zhang), jfjhtb@163.com (F.-J. Jiang).

revolution", transitioning from conventional to unconventional oil and gas. This shift has significantly altered the global energy landscape, with unconventional oil and gas playing a prominent role in the growth of global oil and gas production, and their importance is on the rise (Jarvie et al., 2007; Zou et al., 2019b; Jin et al., 2022). Due to its significant resource potential, shale oil has emerged as a pivotal area within unconventional oil and gas exploration. The commercial development of shale oil resources in North America has catalyzed worldwide shale oil exploration

<sup>\*</sup> Corresponding author.

<sup>\*\*</sup> Corresponding author.

<sup>\*\*\*</sup> Corresponding author.

efforts, prompting accelerated research in shale oil and gas exploration in China as well (Li et al., 2018; Zou et al., 2019a). Chinese shale oil mainly occurs in continental shale formations, such as Yanchang Formation in Ordos Basin, Shahejie Formation in Dongying Sag, Bohai Bay Basin, Lusaogou Formation in Jimsal Sag, Qingshankou Formation in Gulong Sag, the northern Songliao Basin (Li et al., 2015; Hu et al., 2021, 2024a; Guo et al., 2022; Lv et al., 2023), and shale oil resources exhibit great potential. Nevertheless, large-scale production of lacustrine shale oil remains elusive, primarily due to an inadequate comprehension of the occurrence mechanism of retained oil in tight shale formations. Furthermore, compared with Marine shale oil, lacustrine shale oil presents more intricate geological conditions and greater heterogeneity. Additionally, lacustrine shale oil exhibits higher viscosity and lower fluidity (Zhu et al., 2019).

Shale reservoirs are characterized by high density, low porosity, and low permeability, primarily consisting of micro-nano pores (Nelson, 2009; Shao et al., 2018; Xu et al., 2022). Unlike conventional oil and gas, shale oil exhibits in-situ characteristics of selfgeneration and self-retention, undergoing distinct stages during the processes of generation and expulsion. When organic matter begins to generate hydrocarbons, hydrocarbons need to fill pore cracks after meeting the adsorption effect of organic matter and mineral surface, and excess hydrocarbons are discharged outward (Wang et al., 2019; Wu et al., 2022). Hydrocarbons trapped in shale coexist in free, adsorbed and dissolved states, and shale oil mainly exists in free and adsorbed states (Li et al., 2018; Li et al., 2020; Guan et al., 2022; Zhang et al., 2023). Within shale oil systems, adsorbed oil attaches to the surfaces of organic matter and mineral particles or is absorbed by organic matter (Xu et al., 2022; Zhang et al., 2023). This adsorbed oil exhibits low mobility and remains unrecoverable using current extraction techniques. Conversely, free oil predominantly resides in large inorganic pores and fractures, displaying higher fluidity and greater extraction potential (Shao et al., 2018; Liu et al., 2020). Thus, the complexity of shale oil microscopic occurrence primarily stems from the unrecoverable nature of adsorbed oil, which not only impacts the microscopic occurrence, oil content, and mobility of shale oil but also impedes its large-scale exploitation.

Within the shale oil reservoir system, the correlation between the multi-scale topological fracture network and shale oil in various occurrence states (shale oil occurrence mechanism) is highly intricate. This complexity leads to shale oil exhibiting different fluidities depending on its occurrence states (Fleury and Romero-Sarmiento, 2016; Li et al., 2018; Wang et al., 2023). Generally speaking, the mobility of shale oil depends on its occurrence state in shale (Jarvie, 2012; Zou et al., 2019b; Xi et al., 2023). Previous studies have shown that the occurrence state of shale oil is difficult to define, and the conversion conditions between different occurrence states are unclear (Fleury and Romero-Sarmiento, 2016; Cui and Cheng, 2017; Wang et al., 2019; Li et al., 2020; Liu et al., 2020; Zhang et al., 2023). Qualitative and quantitative evaluation of shale oil occurrence characteristics typically involves two main approaches: experimental testing and theoretical simulation. In terms of experimental testing, scanning electron microscope observation and nuclear magnetic resonance are the most commonly used experimental methods to distinguish the occurrence state of shale oil. Compared with scanning electron microscope, which can directly observe the characteristics of oil occurrence, nuclear magnetic resonance experiment can quickly display the fluid state in shale oil by relying on the non-damage characteristics (Li et al., 2020; Zhang et al., 2023; Jiang et al., 2023). Multi-temperature pyrolysis method and two-step pyrolysis method are common methods for quantitative evaluation of shale oil content in different occurrence states (Jarvie, 2012; Jiang

et al., 2016; Li et al., 2018; Guan et al., 2022). In terms of theoretical simulation, predecessors often use molecular dynamics simulation methods in combination with computer technology to reflect occurrence characteristics, but there are great limitations in the establishment of complex components and mineral models of petroleum molecules (Cui and Cheng, 2017; Xu et al., 2022).

With the discovery of micro-nano reservoir space of unconventional oil and gas, the understanding of shale oil occurrence space on a micro-scale has become the core problem of the shale oil occurrence mechanism. Previous studies have shown that micronano pores are the most important occurrence Spaces of shale oil. Li et al. (2020) pointed out that the storage and occurrence states of shale oil in pores of different scales and levels are different, and studied the mechanism of the influence of pore structure on the occurrence characteristics of shale oil. Moreover, it is found that the pore throat size is also an important factor restricting the occurrence and flow of hydrocarbons, shale oil with different occurrence states has different distribution in the pore structure. Recent thermodynamic studies (Akkutlu et al., 2017) have demonstrated that strong fluid-rock interactions within shale oil systems result in notable deviations in fluid properties within nanoscale pores compared to the bulk. Zhang et al. (2014) indicated that hydrocarbon molecules become trapped within pores smaller than the critical threshold (10 nm) due to differences in fluid properties. Wang et al. (2019) analyzed shale oil occurrence by comparing before and after extraction pore structures through theoretical calculations, concluding that shale oil predominantly occupies pores smaller than 100 nm, while adsorbed oil is confined to pores smaller than 5 nm. On the whole, although predecessors have used different technical means to reveal the microscopic occurrence of shale oil, the relevant research and understanding are not uniform (Shao et al., 2018; Li et al., 2020; Zhu et al., 2019; Liu et al., 2020; Wu et al., 2022). Therefore, it is necessary to further study the distribution of oil in micro-nano pores.

The Mahu Sag in the Junggar Basin is renowned domestically and internationally for its abundant hydrocarbon resources (Tao et al., 2019). Over recent years, extensive shale oil explorations have been conducted within the Fengcheng Formation (P<sub>1</sub>f) of the Mahu Sag, resulting in several wells achieving commercial exploitation, thus indicating a promising outlook for shale oil in the region. The P<sub>1</sub>f shale is the oldest high-quality source rock of alkaline lacustrine found so far (Cao et al., 2015; Zhi et al., 2021), and has a unique hydrocarbon generation and occurrence mechanism, which is significantly different from traditional lacustrine shale oil. This paper focuses on investigating the P<sub>1</sub>f shale in Mahu Sag, aiming to clarify the occurrence characteristics of alkali-lake shale oil, reveal the influence and mechanism of various parameters on shale oil occurrence, establish the correlation between the organicinorganic pore network and hydrocarbon occurrence in the alkaline lacustrine environment (the shale oil occurrence mechanism), and advance the theoretical understanding of shale oil enrichment in Alkali Lake.

#### 2. Geological setting

The Junggar Basin is the most important hydrocarbon-bearing basin in the western part of China, located in the northern part of Xinjiang (Tao et al., 2016). According to the basement tectonic basin can be divided into six primary tectonic units (Fig. 1(a) and (b)). Mahu Sag is located in the northernmost part of the central depression of Junggar Basin, and is the most hydrocarbon-rich oil and gas gathering area in the basin (Tang et al., 2021; Zhi et al., 2021; Hu et al., 2024b). Mahu Sag developed along the northwest margin of the Junggar Basin fault zone and formed the present tectonic pattern after multiple tectonic movements (Liu et al., 2016)

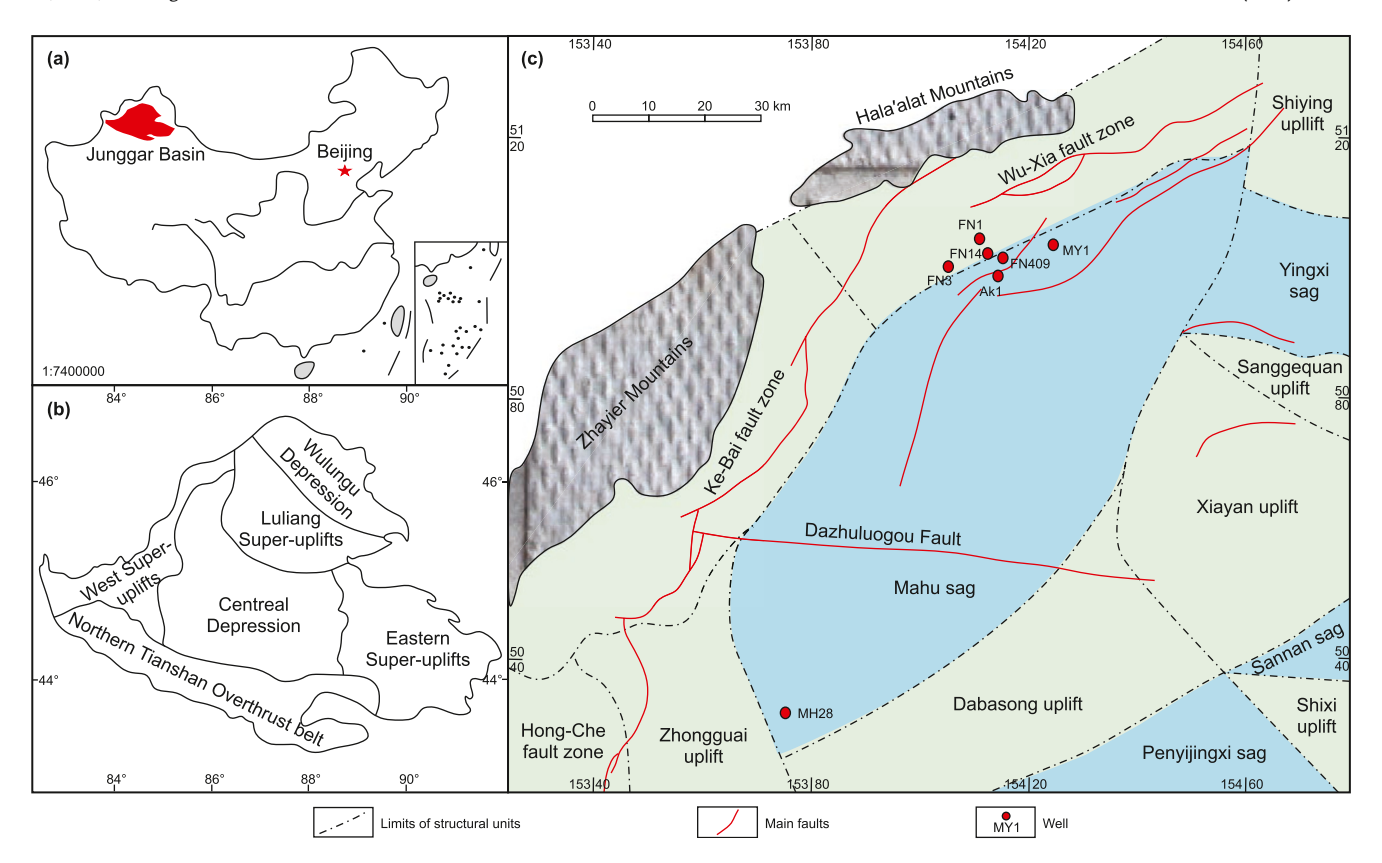


Fig. 1. (a) Geographical location of the Junggar Basin. (b) Major tectonic units of the Junggar Basin. (c) Location of tectonic units and Wells in Mahu Sag (modified from Feng et al. (2020)).

## (Fig. 1(c)).

The stratigraphy of the Mahu Sag is well developed, with Carboniferous-Cretaceous strata deposited from the bottom up (Fig. 2(a)). The target layer of this study is Permian P<sub>1</sub>f, which is a set of alkali-lake sedimentary system (Yu et al., 2018; Cao et al., 2020). From the bottom up, the P<sub>1</sub>f can be divided into the 1st member of the Fengcheng Formation (P<sub>1</sub>f<sub>1</sub>), 2nd member of the Fengcheng Formation (P<sub>1</sub>f<sub>2</sub>) and 3rd member of the Fengcheng Formation (P<sub>1</sub>f<sub>3</sub>) (Fig. 2(b)). During the sedimentary period of P<sub>1</sub>f<sub>1</sub>, there were frequent volcanic activities, mainly composed of bottom volcanic rocks and upper cloudy shale (Guo et al., 2021). P<sub>1</sub>f<sub>2</sub> mainly develops interlayers of evaporite, saline mudstone, and argillaceous siltstone, when the lake has the highest salinity and a large number of alkaline minerals are developed (Yu et al., 2019). During the P<sub>1</sub>f<sub>3</sub> deposition period, terrigenous detrital material increased and mainly developed calcareous mudstone, silty mudstone, and silty mudstone.

#### 3. Samples and methods

The  $P_1f$  in Mahu Sag is the oldest alkali-lacustrine source rock found so far, which has great shale oil exploration prospects. A total of 26 samples were collected from the primary shale oil exploration risk well MY1 and six surrounding Wells, as shown in Fig. 1(c). The microscopic occurrence space and oil content in different occurrence states of shale oil were characterized by comprehensive method. TOC, rock pyrolysis, multi-step pyrolysis, XRD analysis, scanning electron microscopy, porosity measurement and soxhlet extraction were carried out on samples. On the basis of petrographic classification, 8 representative shale samples were selected for gas adsorption and two-dimensional nuclear magnetic

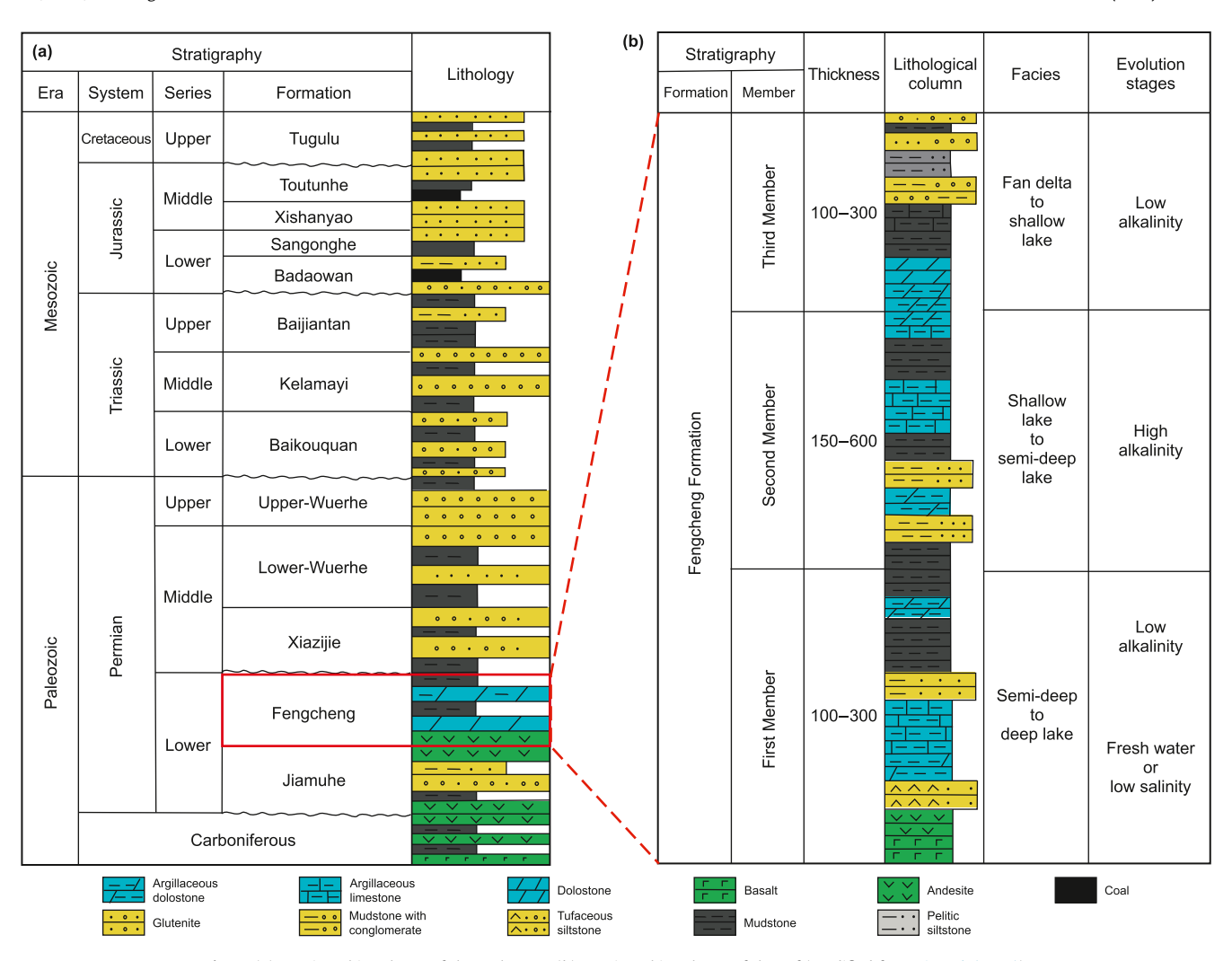
resonance experiments after extraction.

## 3.1. TOC, Rock-Eval pyrolysis and soxhlet extraction

The TOC of 26 samples was analyzed using a CS-230HC analyzer. Initially, the samples were crushed to 100 mesh and then rinsed in a crucible with 5% dilute hydrochloric acid for 2 days to eliminate inorganic carbon. Subsequently, the samples underwent repeated rinsing with distilled water until neutral pH was achieved, followed by drying. After drying, iron and tungsten were introduced into the crucible as combustion aids, and the samples were incinerated to obtain experimental results. The surface of the sample was cleaned and crushed to 200 mesh. Subsequently, dichloromethane was employed as a solvent for laboratory extraction over a three-day period until no fluorescence was observed, effectively removing all soluble organic compounds, including heavy hydrocarbons (Li et al., 2018). The raw and extracted core powders were pyrolyzed with Rock-evalII apparatus. The samples were heated to 600 °C in helium atmosphere, generating three parameters simultaneously:  $S_1$ ,  $S_2$ , and  $T_{\text{max}}$ .

#### 3.2. XRD, FE-SEM and porosity measurement

The sample was ground into 300 mesh, the powder was pressed into the container by back pressure to maintain a uniform surface, and then XRD analysis was performed using the ZJ207 Bruker D8 diffractometer at a temperature of 24 °C and a humidity of 35%, where the X-ray scanning range was 3°–85°, the aperture was 1 mm, and the scanning speed was 4°/min. During the scanning electron microscope experimental analysis, part of the sample was mechanically ground, and the treated sample was made into a size



 $\textbf{Fig. 2. (a)} \ Stratigraphic \ column \ of \ the \ Mahu \ Sag. \textbf{(b)} \ Stratigraphic \ column \ of \ the \ P_1f \ (modified \ from \ Li \ et \ al. \ (2021)).$ 

of  $10 \times 5 \times 1.5$  mm (width, height and length), and then installed in resin after polishing. In order to further improve the image quality, the surface of the sample was gilded and observed by Sigma-500 scanning electron microscope. To measure sample porosity, 26 core columns (2.5 cm in diameter and 2.5 cm in length) were cleaned with benzene and alcohol in a Soxhlet extractor for more than a month until the extract was colorless. Then, the sample was dried, and the rock physical properties of the core column were measured and analyzed, and the porosity was determined by helium injection method according to SY/T5336-2006 standard.

#### 3.3. Multi-step pyrolysis

The multi-step pyrolysis method is an improvement on the Rock-Eval 6 pyrolytic analysis method.  $S_{1-1}$  is tested at 200 °C for 1 min, and then the temperature is raised to 350 °C at 25 °C/min, and  $S_{1-2}$  is tested at constant temperature for 1 min. Then the temperature was raised at 25 °C/min to 450 °C, and the temperature was kept constant for 1 min to test  $S_{2-1}$ , and finally the temperature was raised at 25 °C/min to 600 °C to test  $S_{2-2}$ . The specific experimental procedure was referred to Jiang et al. (2016).

## 3.4. Gas adsorption

The low-temperature gas adsorption experiment was conducted

using the Autosorb iQ instrument. Prior to the experimental tests, the samples underwent preprocessing, involving cleaning of the sample surfaces and grinding them to an 80-mesh size. A quantity of 6–10 g of powder sample was then placed in an oven at 110 °C for 12 h to degas, ensuring the samples were thoroughly dried and any volatile substances were removed. The  $N_2$  adsorption experiment was carried out at a temperature of 77.35 K, with relative pressures  $(P/P_0)$  ranging from 0.005 to 0.996. The pore parameters were calculated using the BET theory and the BJH model. The  $CO_2$  adsorption experiment was conducted at a temperature of 273 K, with relative pressures  $(P/P_0)$  ranging from 0.00001 to 0.032. The pore parameters were calculated using the Density Functional Theory (DFT). For the specific experimental procedures, refer to Liu et al. (2017).

#### 3.5. Two-dimensional nuclear magnetic resonance of highfrequency

The 2D high-frequency nuclear magnetic resonance (NMR) experiment was conducted using the MesoMR23-060H-I instrument. The experimental magnet temperature was maintained at 32 °C, with the device operating at a frequency of 21.36 MHz. The main magnetic field strength of the equipment was 0.5 T. During the testing process, the IR-CPMG sequence was employed to measure the Nuclear Magnetic Resonance (NMR) T<sub>1</sub>-T<sub>2</sub> relaxation

spectra. The CPMG pulse sequence, with its advantage of mitigating the effects of internal magnetic field inhomogeneities, is more suitable for the experimental procedure compared to the Free Induction Decay (FID) pulse sequence. The test parameters were as follows: Echo Time (TE) of 0.1 ms; Number of Scans (NS) set to 64; Waiting Time (WT) of 2000 ms: Number of Echoes (NE) amounted to 10000; and the inversion was repeated 61 times. An extremely low Echo Time (TE) of 0.1 ms enables the detection of all fluids present in pores, as well as any fraction of immobile or "pseudosolid" protons. The T<sub>1</sub>-T<sub>2</sub> NMR spectra were acquired using 24 logarithmically spaced inversion recovery steps, and the inversion was performed employing a Fast Laplace Inversion Transform (Kausik et al., 2016). This approach ensures comprehensive characterization of the pore structure and fluid distribution within the sample, even in complex systems where both bound and free fluids coexist.

#### 4. Results and discussion

#### 4.1. Petrology and mineral compositions

The  $P_1f$  in Mahu Sag has diverse provenance and complex mineral composition. Terrigenous clastic, carbonate, and volcanic materials are all deposited. According to the results of X-ray diffraction (XRD) (Table 1), the main mineral types of the  $P_1f$  are quartz (0~51.8%, average 19.5%), dolomite (0~51.9%, average 23.4%), calcite (0~62.9%, average 18.7%) and feldspar (2.4%~39.2%, average 18.3%), followed by clay minerals (0~31.1%, average 7.2%), a small amount of pyrite (0~17.5%, average 5.1%) and gypsum. Compared with typical shale reservoirs at home and abroad, the shale of  $P_1f$  is special in the characteristics of high carbonate felsic minerals and low clay minerals. Based on the classification of mineral components, the  $P_1f$  primarily consists of felsic shale, dolomitic shale, lime shale, and mixed shale (Fig. 3).

The developmental characteristics of various types of minerals can be observed under FE-SEM. Quartz exhibits a high degree of dimorphism and is self-generated as mineral particles on the particle surface (Fig. 4(a)). The carbonate minerals are idiomorphic

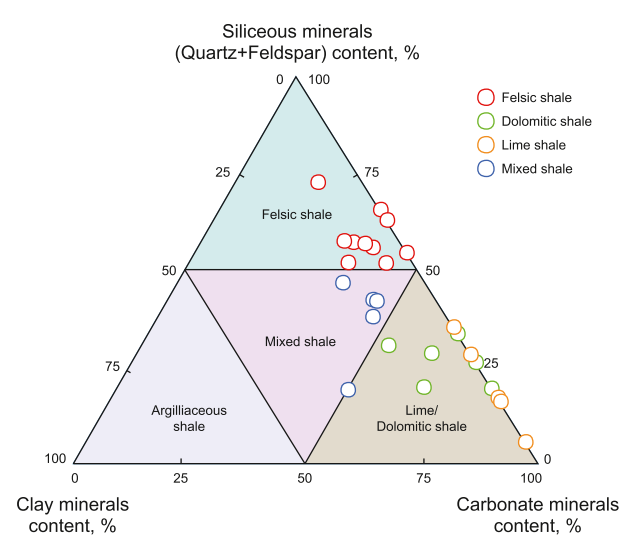


Fig. 3. Triangular diagram of shale mineral composition.

crystals, mainly dolomite, with a rhombic or subrhombic shape (Fig. 4(b)). Albite exhibits a plate-like distribution, and the clay minerals are mainly dominated by honeycomb I/S and lamellar illite, with a directional distribution of illite (Fig. 4(c) and (d)). Pyrite is often distributed as spherulitic aggregates (Fig. 4(e)), and alkaline minerals such as reedmergnerite were observed in abundance under FE-SEM (Fig. 4(f)).

#### 4.2. Geochemical characteristics

# 4.2.1. Abundance, type and thermal maturity of organic matter

The geochemical parameters of shale samples from  $P_1f$  are shown in Table 2. The organic matter content ranges from 0.14% to 2.33%, with an average value of 1.04%. The value of  $S_1$  ranges from 0.35 to 8.39 mg/g, with an average value of 1.68 mg/g. The value of  $S_2$  ranges from 0.2 to 12.43 mg/g, with an average value of 3.23 mg/g

**Table 1**Mineral compositional characteristics of shale in the P<sub>1</sub>f.

Sample no.	Well	Depth, m	Lithofacies	Quartz, %	Feldspar, %	Plagioclase, %	Calcite, %	Dolomite, %	Clay, %	Pyrite, %	Others, %
ZGR-1	MY1	4580.34	felsic shale	46.8	0	6.1	33.3	0	0	13.7	0.1
ZGR-2	MY1	4910.63	felsic shale	47	11.4	12.8	2.6	0	9.4	0	16.8
ZGR-3	MY1	4911.77	felsic shale	17.8	11.1	23.5	3.1	21.3	6	3	14.2
ZGR-4	MY1	4708.88	felsic shale	51.3	2.7	11.1	3.8	26.7	0	4.4	0
ZGR-5	MY1	4744.9	felsic shale	28.3	5.8	22.1	14.1	11.8	9.7	6.7	1.5
ZGR-6	MY1	4812.58	felsic shale	51.8	6.3	4.1	14	18.8	0	4.9	0.1
ZGR-7	MY1	4807.89	felsic shale	28.4	7.8	18.4	8.9	17	7.4	8.7	3.4
ZGR-8	FN1	4321	felsic shale	22.4	11.6	12	13.9	21.2	7.9	5.1	5.9
ZGR-9	MH28	4843.3	felsic shale	27.6	4.7	23.9	8.8	13.7	11.4	5.3	4.6
ZGR-10	MH28	4933.5	felsic shale	15.9	4.5	25.7	14.3	14	15.8	5.6	4.2
ZGR-11	MY1	4594.63	dolomitic shale	9.6	6.8	11.8	28.9	28.9	7.8	6.2	0
ZGR-12	MY1	4710.99	dolomitic shale	17.2	2.3	12.4	28	30.1	0	4.5	5.5
ZGR-13	MY1	4605.54	dolomitic shale	16.9	4.9	8.5	0	48.3	15.9	5.6	0
ZGR-14	FN409	4527.95	dolomitic shale	2.9	2	14.1	31.5	41.6	0	4.4	3.5
ZGR-15	FN14	4166.05	dolomitic shale	10.6	5.4	9.9	16.4	51.9	0	5.8	0
ZGR-16	AK1	5663.6	dolomitic shale	0.9	7.9	1.7	11.1	11.2	7.3	0	59.9
ZGR-17	MY1	4694.31	lime shale	11.7	4.5	10.9	33.1	31.6	0	8.2	0
ZGR-18	FN1	4362.88	lime shale	10.8	11.3	10.2	42.2	10.7	0	7.6	7.2
ZGR-19	FN3	4147.5	lime shale	0	0	6.6	62.9	30.4	0	0	0.1
ZGR-20	AK1	5666	lime shale	0	7.4	3.9	41.2	6.4	0	0	41.1
ZGR-21	AK1	5667.8	lime shale	0	7.9	4.6	45	12.4	0	17.5	12.6
ZGR-22	MY1	4772.01	mixed shale	11.2	11.4	12.8	3	30.6	14.6	8.4	8
ZGR-23	FN3	3955.58	mixed shale	0.7	4.9	34.3	13	20.5	12.1	0	14.5
ZGR-24	FN14	4033.1	mixed shale	17.4	0	2.4	14.2	35	31.1	0	0
ZGR-25	FN14	4082.5	mixed shale	25	2.6	14.8	0	42.9	12.7	2	0
ZGR-26	FN14	4109.3	mixed shale	34	4.3	8.5	0	31.9	17.5	3.8	0

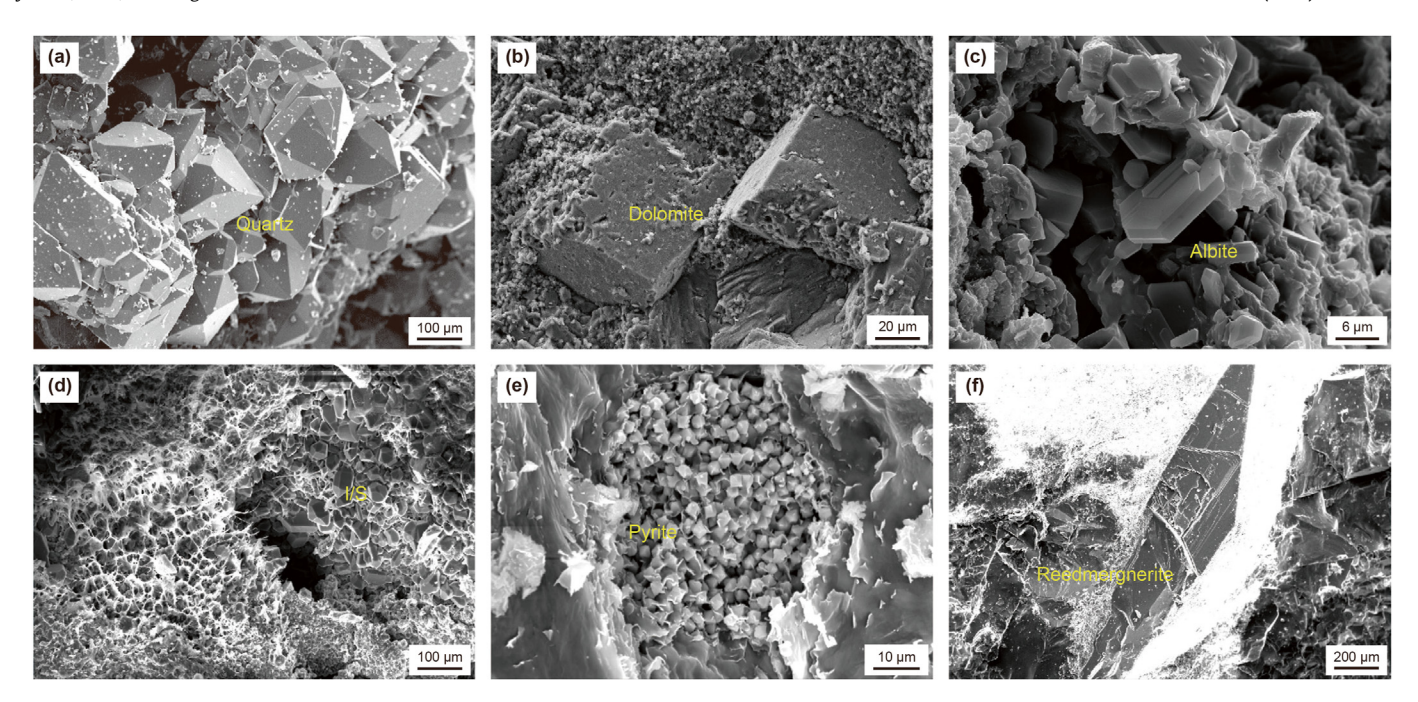


**Fig. 4.** Petrographic characteristics under SEM. **(a)** Authigenic quartz aggregate, X72, 4808.62 m. **(b)** Rhombic dolomite crystals MY1, 4713.79 m. **(c)** Tabular albite, MY1, 4612.31 m. **(d)** Honeycomb I/S, JL34, 3151.78m. **(e)** Pyrite aggregate, JL35, 4226.62 m. **(f)** Reedmergnerite, FN7, 4588.84 m.

**Table 2** Geochemical parameters of P<sub>1</sub>f.

Sample no.	Well	Depth, m	TOC, wt%	Rock-Eval	(Original)		Rock-Eval (Extracted)		
				$\overline{S_1}$	$S_2$	$T_{\max}$	$S_1$	$S_2$	$T_{ m max}$
ZGR-1	MY1	4580.34	0.587	0.86	1.52	438	0.07	0.71	441
ZGR-2	MY1	4910.63	1.356	8.39	5.4	421	0.02	0.25	442
ZGR-3	MY1	4911.77	1.004	6.91	3.65	414	0.02	0.41	441
ZGR-4	MY1	4708.88	0.766	3.21	3.03	421	0.02	0.53	437
ZGR-5	MY1	4744.9	1.134	1.98	3.28	428	0.04	1.67	437
ZGR-6	MY1	4812.58	0.848	0.97	2.33	436	0.04	1.17	444
ZGR-7	MY1	4807.89	0.859	0.57	2.16	435	0.04	1.24	442
ZGR-8	FN1	4321	0.654	1.09	2.15	421	0.03	0.48	426
ZGR-9	MH28	4843.3	0.275	0.43	0.41	430	0.04	0.25	435
ZGR-10	MH28	4933.5	0.407	0.74	0.47	351	0.05	0.15	429
ZGR-11	MY1	4594.63	2.328	4.03	9.01	435	0.1	4	443
ZGR-12	MY1	4710.99	0.937	0.6	2.48	436	0.05	1.95	440
ZGR-13	MY1	4605.54	0.919	0.99	1.69	438	0.05	0.94	439
ZGR-14	FN409	4527.95	0.311	0.53	0.56	418	0.05	0.26	426
ZGR-15	FN14	4166.05	2.055	1.28	10.58	439	0.05	9.84	442
ZGR-16	AK1	5663.6	0.382	0.35	0.2	403	0.03	0.19	401
ZGR-17	MY1	4694.31	1.432	1.15	3.72	436	0.03	2.77	442
ZGR-18	FN1	4362.88	0.813	0.83	3.07	432	0.06	2.02	440
ZGR-19	FN3	4147.5	2.003	1.7	3.89	432	0.03	1.17	436
ZGR-20	AK1	5666	0.409	0.73	0.47	399	0.02	0.24	422
ZGR-21	AK1	5667.8	0.413	0.67	0.52	401	0.04	0.31	1
ZGR-22	MY1	4772.01	1.930	0.57	12.43	445	0.04	12.31	447
ZGR-23	FN3	3955.58	1.019	2.48	2.55	410	0.03	0.41	430
ZGR-24	FN14	4033.1	0.135	0.35	0.24	368	0.06	0.14	372
ZGR-25	FN14	4082.5	2.287	1.29	4	434	0.04	1.15	441
ZGR-26	FN14	4109.3	1.829	0.98	4.2	437	0.05	1.43	437

Note: The units of  $S_1$  and  $S_2$  are mg HC/g Rock, and the unit of  $T_{\rm max}$  is  ${}^{\circ}C$ .

g.  $P_1f$  is an alkali-lacustrine sedimentary system with a high hydrocarbon conversion rate, which can be a good source rock and generate a large amount of hydrocarbons at a TOC greater than 0.6% (Li et al., 2015; Cao et al., 2015; Tao et al., 2019; Tang et al., 2021). The TOC vs.  $S_1$  plot shows that more than half of the samples are located in the "oil crossing zone" (Jarvie, 2012) with an oil saturation index (OSI) greater than 100 mg HC/g Rock, which has a good potential for oil production (Fig. 5(a)). The samples on the HI and

 $T_{\rm max}$  plots were widely distributed in type I and II kerogen regions, with type II kerogen being the dominant one (Fig. 5(c)), and the TOC vs.  $S_1$  plot also showed that the majority of the samples were located in the type II kerogen region (Fig. 5(b)). The P<sub>1</sub>f shale contains a large amount of soluble organic matter, and the  $T_{\rm max}$  value is polluted by heavy oil or asphalt, which cannot accurately reflect the thermal maturity of organic matter (Katz and Lin, 2021; Guo et al., 2022). After extraction with organic solvent,  $T_{\rm max}$  significantly

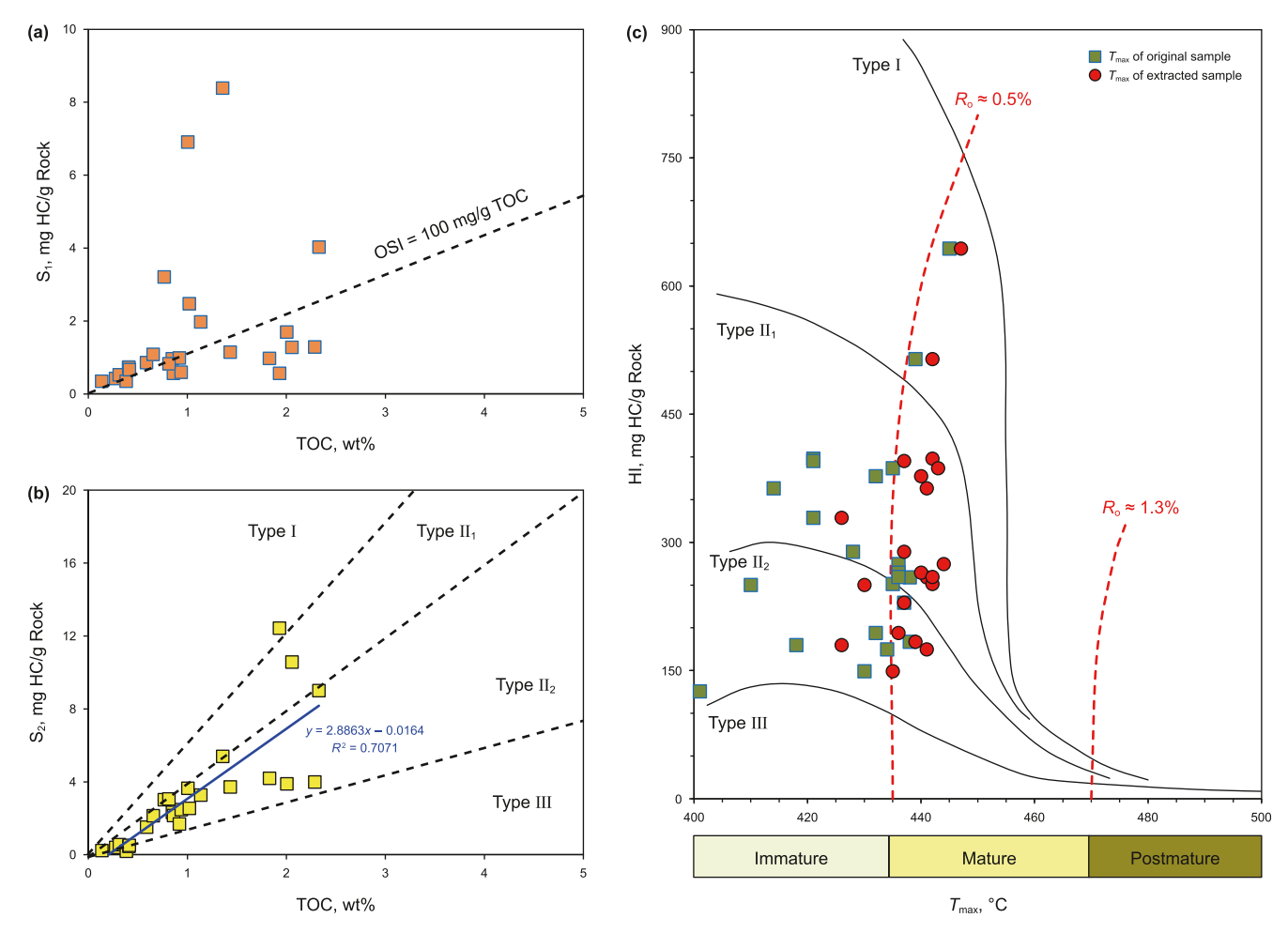


**Fig. 5.** Geochemical characteristics of the  $P_1$ f. (a) Correlation of shale TOC content with  $S_1$ . (b) Correlation of shale TOC content with  $S_2$ . (c) Correlation between  $T_{\text{max}}$  and hydrogen index (HI) before and after extraction.

increases. The extracted  $T_{\text{max}}$  value indicates that  $P_1f$  shale is in the mature stage, with organic matter located within the oil generation window, consistent with previous research results (Tang et al., 2021; Li et al., 2021; Zhang et al., 2023).

#### 4.2.2. Comparison of pyrolysis results before and after extraction

The pyrolysis parameters of the extracted samples are shown in Table 2. The content of  $S_{1\text{extracted}}$  after solvent extraction was lower, ranging from 0.02 to 0.1 mg/g, with an average of 0.04 mg/g. The S<sub>2extracted</sub> value after solvent extraction ranged from 0.14 to 12.31 mg/g, with an average of 1.77 mg/g. A comparison of the geochemical results before and after extraction shows (Fig. 6(a)–(c)) that the contents of  $S_1$  and  $S_2$  in the samples after extraction were reduced to different degrees, and the average loss of  $S_1$  and  $S_2$  in the samples before and after extraction was 95% and 51%, respectively. The greatest reduction of  $S_1$  after extraction indicates that  $S_1$  mainly consists of soluble organic matter, and the partial reduction of S<sub>2</sub> after extraction suggests that some high molecular weight and heavy hydrocarbons were successfully removed from pyrolytic hydrocarbons during solvent extraction (Dembicki et al., 1983; Jarvie et al., 2007; Li et al., 2018). In addition, the  $T_{\text{max}}$  value of the sample increases generally after extraction, which is since the pyrolysis hydrocarbon S<sub>2</sub> before solvent extraction contains some heavy hydrocarbons and some nonhydrocarbon substances, and the pyrolysis temperature is low when the peak of  $S_2$  appears. The solvent extraction process eliminates the "carry-over effect" and increases the  $T_{\text{max}}$  value (Abrams

#### et al., 2017; Li et al., 2018; Zhu et al., 2019; Katz and Lin, 2021).

Pyrolysis parameter  $S_1$  refers to the free and volatile hydrocarbons measured by the pyrolysis experiment at 300 °C, which cannot reflect the heavy hydrocarbon components in oil. Therefore, using pyrolysis hydrocarbon  $S_1$  to characterize shale oil content will lead to a serious underestimation of shale oil potential (Shao et al., 2018; Hu et al., 2018; Wang et al., 2022). While numerous studies have investigated the characterization of oil content in shale using two-step pyrolysis, the sources of  $S_1$  extracted in the samples are not consistently understood (Jarvie, 2012; Han et al., 2015; Li et al., 2018). In this study, it is considered that  $S_{1\text{extracted}}$  is the hydrocarbon component originally enclosed in the nanoscale pores of shale during the secondary pyrolysis process after solvent extraction. Therefore, the method proposed by Li et al. (2018) is used to calculate the total oil content of P<sub>1</sub>f shale. There is a good positive correlation between the corrected total oil content and the original pyrolyzed hydrocarbon  $S_1$  ( $R^2 = 0.93$ ), and the total oil content increases to 1.6 times that of the original pyrolyzed hydrocarbon S<sub>1</sub> (Fig. 6(d)).

#### 4.3. Pore types and morphologies

Shale reservoir space is complex and exhibits significant heterogeneity, serving as the primary occurrence space for shale oil and gas. SEM analysis reveals the presence of numerous micro and nanopores within P<sub>1</sub>f shale. Based on pore genesis, the pore network of P<sub>1</sub>f shale can be categorized into intergranular pores,

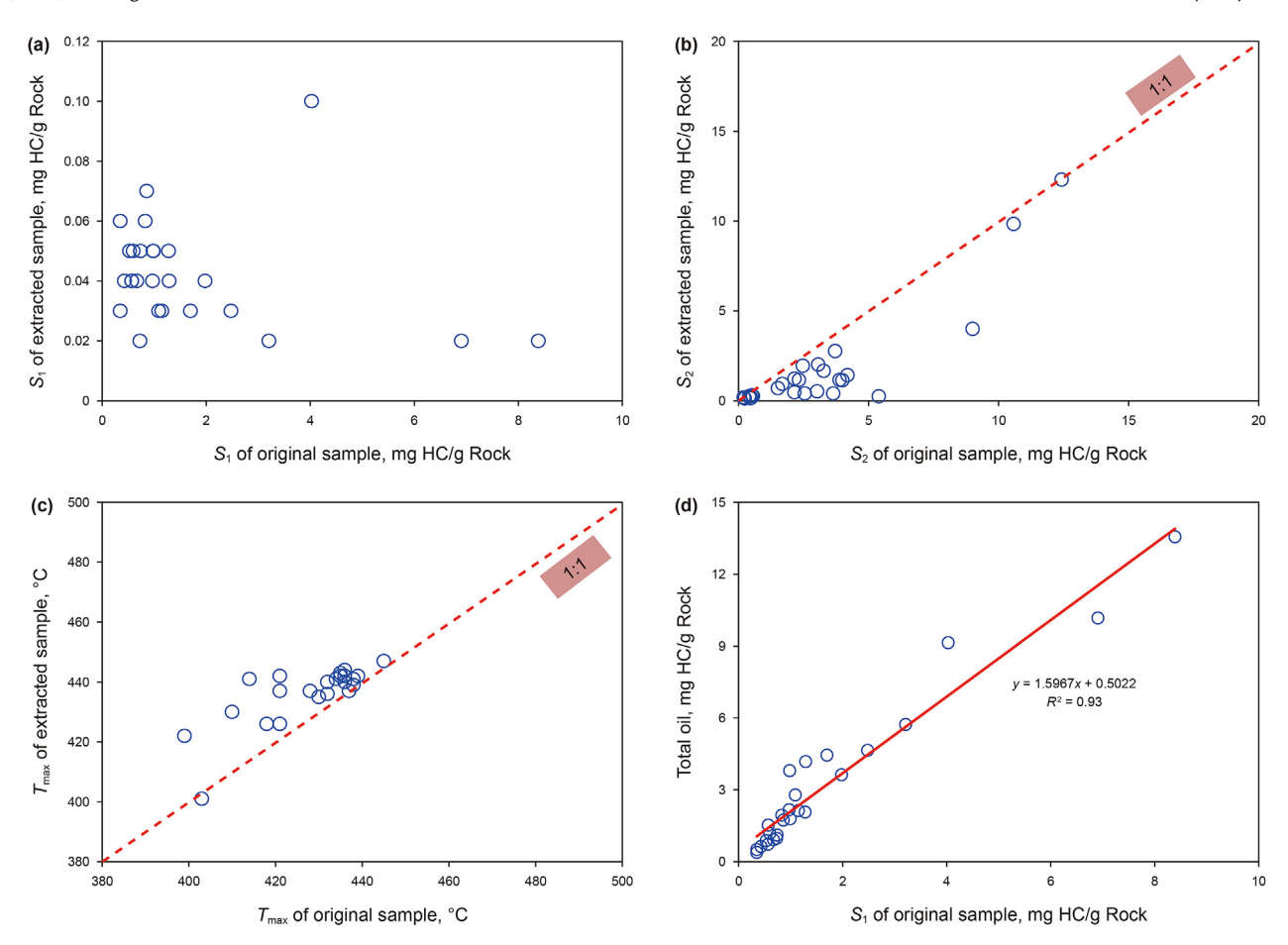


**Fig. 6.** (**a–c**) Comparison of organic geochemical parameters (free hydrocarbon [ $S_1$ ], pyrolysis hydrocarbon [ $S_2$ ], and maximum pyrolysis peak temperature [ $T_{max}$ ]) before and after extraction. (**d**) The relationship between total oil content and free hydrocarbons [ $S_1$ ].

intragranular pores, organic pores, and microfractures (Loucks and Ruppel, 2007).

Intergranular pores are generally developed, mainly between mineral particles or clay minerals. The pore morphology is triangular or slit, and the pore size distribution ranges from tens of nanometers to several microns (Fig. 7(a)-(c)). These pores open along the edges of composite particles and are connected to adjacent pores under the protection of rigid minerals. Intragranular pores are widely developed in dolomitic and lime shale, mainly related to feldspar, carbonate minerals, clay minerals, and pyrite (Fig. 7(d) and (e)). The dissolution pores of unstable minerals such as dolomite and feldspar, which are affected by hydrocarbon generation by organic matter, are generally large in pore size and irregular in shape. The lamellar clay minerals such as I/S and illite develop intercrystalline pores of clay minerals (Fig. 7(g)), whose pore sizes are generally less than 100 nm due to clay expansion and adsorption, which are more developed in mixed shale. Pyrite is mainly distributed in spherulite aggregates, and there are a large number of pyrite intercrystalline pores between the crystals (Fig. 7(f)), the pore size is usually between a few nanometers to tens of nanometers, and the connectivity within the mineral aggregates is good, but the aggregate is relatively isolated and the overall connectivity is poor. Organic matter pores are mainly developed in the interior of organic matter (Fig. 7(h)). Organic matter pores are bubble-like and isolated from each other. Organic pore development in P<sub>1</sub>f shale is relatively small, and a small amount of organic pore development in felsic shale and dolomitic shale. Due to the high content of brittle minerals in the shale of P<sub>1</sub>f, microfractures

are widely developed under SEM, and the fracture width is generally micron (Fig. 7(i)). These microfractures not only provide reservoir space but also provide key channels for oil and gas migration. Generally, matrix pores and microfractures related to inorganic minerals are the predominant pore types in  $P_1f$ .

#### 4.4. Occurrence characteristics of shale oil

#### 4.4.1. Occurrence space

The shale oil resource potential of  $P_1f$  is huge, with predominantly micro-nano pores. When a large number of shale hydrocarbons are generated, the larger the shale reservoir space, the more favorable the reservoir oil and gas. However, the storage and occurrence states of shale oil in pores of different scales and levels vary (Wang et al., 2019; Liu et al., 2020). To reveal the distribution characteristics of shale oil in different occurrence states, gas adsorption and Soxhlet extraction were combined to explore the shale oil occurrence space in this study,

Fig. 8 shows the characteristics of  $N_2$  adsorption and desorption isotherms of typical samples from  $P_1f$  after extraction. The nitrogen adsorption and desorption isotherms after extraction are significantly higher than those of original samples before extraction. Pore space formerly occupied by shale oil is freed up. After extraction, the hysteresis rings became larger as a whole, and some hysteresis rings were dominated by slit pores (H3) without any change in shape (Fig. 8(a), (b), (d)), while the other hysteresis rings changed from slit pores (H3) to ink bottle pores (H2) (Fig. 8(c)). In addition, when the relative pressure  $P/P_0$  is close to 1, the adsorption amount

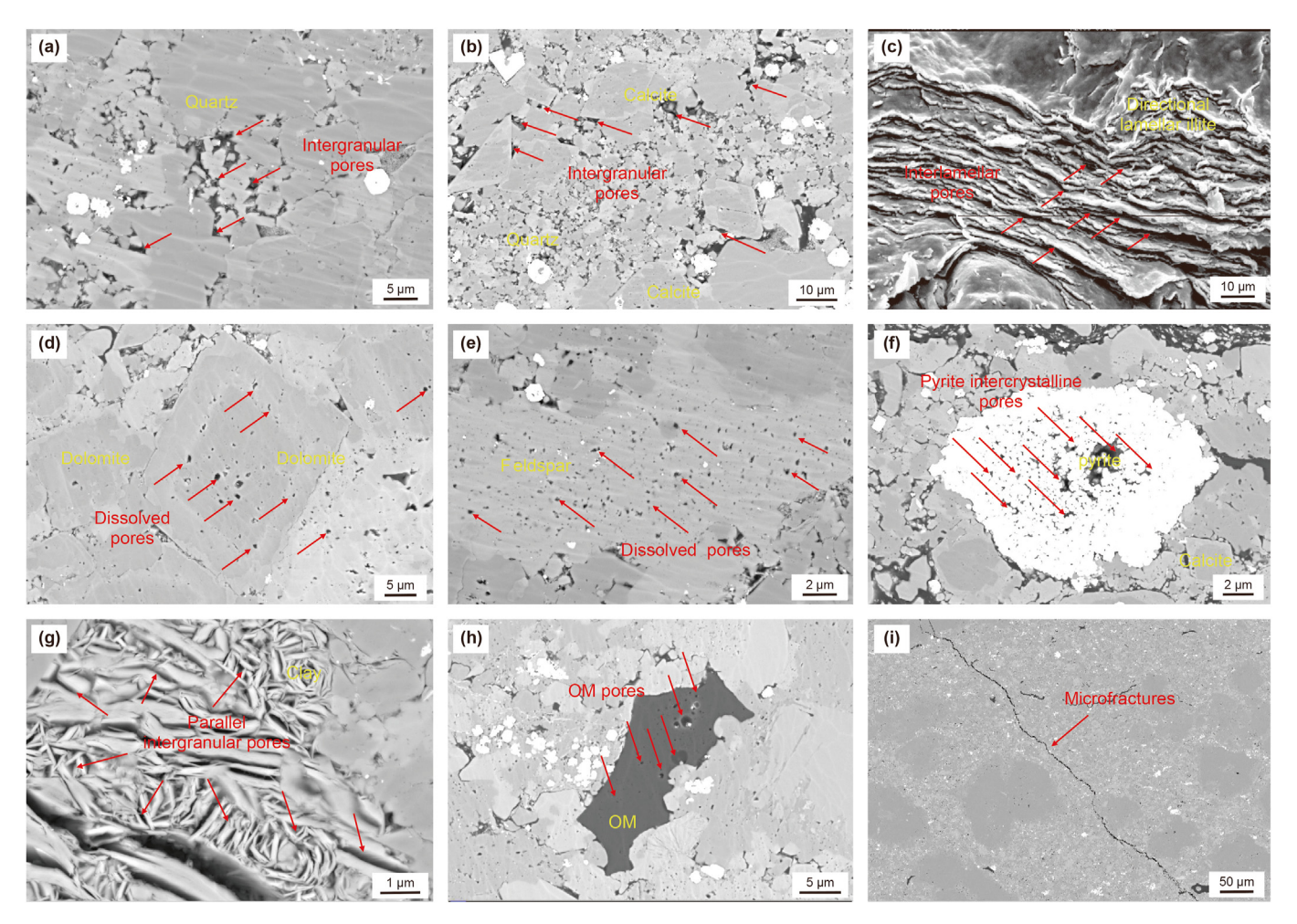
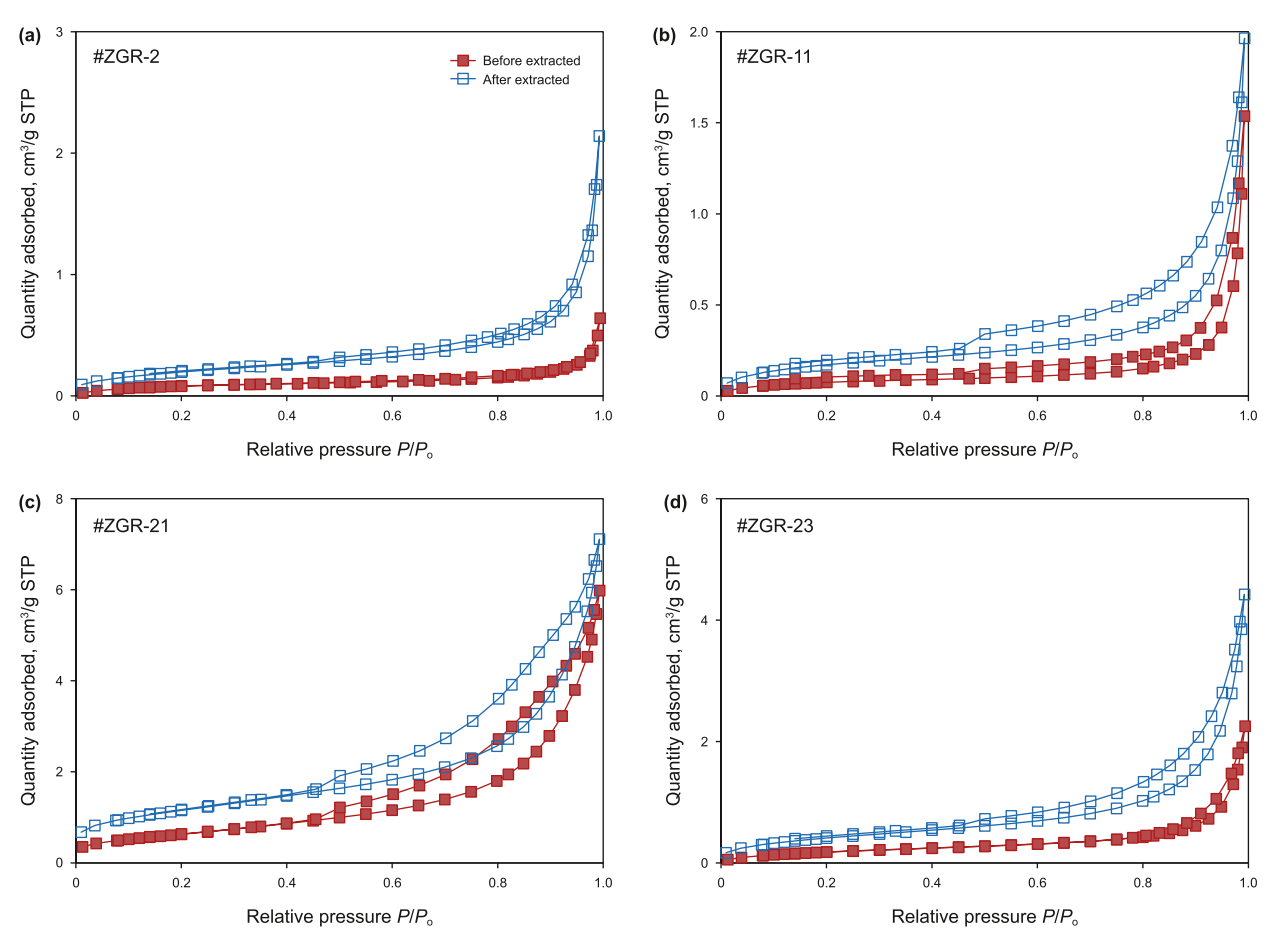


**Fig. 7.** Pore characteristics of P<sub>1</sub>f under SEM. (a) Rigid mineral intergranular pores, MY1, 4594.63 m. (b) Calcalite intergranular pores, MY1, 4594.63 m. (c) Oriented lamellar illite interlayer pores, FN1, 4321.0 m. (d) Carbonate mineral solution pores, MY1, 4594.63 m. (e) Dissolved pores in feldspar, MY1, 4744.9 m. (f) Pyrite intercrystalline pores, FN2, 4041.8 m. (g) Parallel intercrystalline pores between clay minerals, FN14, 4031.1 m. (h) Organic pores, FN1, 4340.0 m. (i) Microfractures, MY1, 4065.54 m.

of nitrogen increases significantly, indicating that the extracted oil or asphalt can occupy part of the larger pore space.

There are significant changes in the pore structure of the shale before and after extraction (Table 3). The pore volume of the original sample is 0.0007-0.0062 cm<sup>3</sup>/g, with an average value of 0.0027 cm<sup>3</sup>/g. The pore volume of the extracted sample is 0.0013-0.0068 cm<sup>3</sup>/g, with an average value of 0.0036 cm<sup>3</sup>/g. The specific surface area of the original sample is  $0.1397-1.1689 \text{ cm}^2/\text{g}$ . The average value was 0.5759 cm<sup>2</sup>/g, and the specific surface area of the extracted sample was 0.3186-1.528 cm<sup>2</sup>/g, with an average value of 0.9389 cm<sup>2</sup>/g. The pore volume and specific surface area of the extracted sample increased significantly, with the pore volume increased by about 1.6 times (up to 2.6 times) and the specific surface area increased by 2.3 times (up to 5.1 times) compared with the original sample. The significant change in pore structure after extraction is due to the release of pore space occupied by residual hydrocarbons by organic solvents, which exposes pore volume and specific surface area. Fig. 9 shows the distribution histogram of PSD with pore volume and specific surface area of shale samples before and after extraction. The PSD histogram of the samples before and after extraction has similar distribution characteristics, and the retained oil exists in the range of several nanometers to several hundred nanometers. The increment of pore volume and specific surface area in different pore diameter ranges before and after extraction is analyzed. The increment of pore volume with a

diameter larger than 10 nm is 26 times that with a diameter smaller than 10 nm, accounting for 80% of the total pore volume increment. On the contrary, the increment of specific surface area with a diameter less than 10 nm is 10 times that with a diameter larger than 10 nm, accounting for 85% of the total pore volume increment. Therefore, it's evident that the increase in pore volume before and after extraction is mainly contributed by pores with diameters larger than 10 nm, and the increase in specific surface area is mainly contributed by pores with diameters smaller than 10 nm, especially those with diameters in the range of 0.5-1.0 nm. Notably, shale oil predominantly exists in free and adsorbed states. Large pores provide sufficient pore volume for free oil enrichment, whereas small pores afford sufficient surface area for adsorbed oil accumulation (Cui and Cheng, 2017; Li et al., 2017; Shao et al., 2018; Zhang et al., 2021). According to the relationship between pore structure increment of different scales and shale oil content of different occurrence states before and after extraction, the total oil content is negatively correlated with the pore volume increment of pores with a diameter less than 10 nm and positively correlated with the pore volume increment of pores with a diameter greater than 10 nm (Fig. 10(a) and (b)). This indicates that the present shale oil is mainly controlled by pores larger than 10 nm in diameter. The increment of specific surface area with a diameter less than 10 nm showed a positive correlation with adsorbed oil content (Fig. 10(c)), and the increment of pore volume with a diameter greater than



 $\textbf{Fig. 8.} \ \ \text{Comparison of N$_2$ adsorption-desorption isotherms of the representative samples before and after extraction.}$ 

Sample no.	State	Pore volume, cm <sup>3</sup> /g			Proportion, %		Specific surface area, m <sup>2</sup> /g			Proportion, %	
		<10 nm	>10 nm	Total	<10 nm	>10 nm	<10 nm	>10 nm	Total	<10 nm	>10 nm
ZGR-2	Before extracted	0.00029	0.00059	0.00088	32.69	67.31	0.1301	0.0246	0.1547	84.08	15.92
	After extracted	0.00030	0.00200	0.00231	13.17	86.83	0.6080	0.0888	0.6967	87.26	12.74
	Increment	0.00002	0.00141	0.00143	1.12	98.88	0.4779	0.0641	0.5420	88.17	11.83
ZGR-3	Before extracted	0.00027	0.00130	0.00157	17.09	82.91	0.3214	0.0601	0.3815	84.25	15.75
	After extracted	0.00029	0.00283	0.00312	9.25	90.75	0.7220	0.0933	0.8152	88.56	11.44
	Increment	0.00002	0.00153	0.00155	1.29	98.71	0.4006	0.0332	0.4337	92.35	7.65
ZGR-11	Before extracted	0.00006	0.00160	0.00166	3.56	96.44	0.0541	0.0856	0.1397	38.73	61.27
	After extracted	0.00032	0.00210	0.00241	13.07	86.93	0.5992	0.1049	0.7041	85.10	14.90
	Increment	0.00026	0.00050	0.00075	33.92	66.08	0.5451	0.0193	0.5644	96.58	3.42
ZGR-14	Before extracted	0.00077	0.00466	0.00543	14.24	85.76	0.8212	0.3477	1.1689	70.25	29.75
	After extracted	0.00101	0.00521	0.00622	16.22	83.78	0.9728	0.3663	1.3391	72.65	27.35
	Increment	0.00024	0.00056	0.00079	29.76	70.24	0.1516	0.0186	0.1702	89.08	10.92
ZGR-17	Before extracted	0.00020	0.00139	0.00159	12.66	87.34	0.4393	0.0661	0.5055	86.92	13.08
	After extracted	0.00067	0.00154	0.00222	30.40	69.60	0.7153	0.0832	0.7984	89.58	10.42
	Increment	0.00047	0.00016	0.00063	75.20	24.80	0.2759	0.0171	0.2930	94.18	5.82
ZGR-21	Before extracted	0.00139	0.00485	0.00624	22.23	77.77	0.8437	0.1641	1.0078	83.72	16.28
	After extracted	0.00146	0.00535	0.00681	21.42	78.58	1.1078	0.2033	1.3111	84.49	15.51
	Increment	0.00007	0.00050	0.00057	12.57	87.43	0.2641	0.0392	0.3034	87.07	12.93
ZGR-22	Before extracted	0.00018	0.00058	0.00075	23.54	76.46	0.2049	0.0338	0.2387	85.85	14.15
	After extracted	0.00022	0.00109	0.00131	16.78	83.22	0.2667	0.0519	0.3186	83.71	16.29
	Increment	0.00004	0.00052	0.00056	7.69	92.31	0.0618	0.0181	0.0799	77.33	22.67
ZGR-23	Before extracted	0.00050	0.00368	0.00418	11.93	88.07	0.5785	0.4315	1.0101	57.28	42.72
	After extracted	0.00053	0.00445	0.00497	10.58	89.42	0.8757	0.6524	1.5280	57.31	42.69
	Increment	0.00003	0.00077	0.00080	3.52	96.48	0.2971	0.2208	0.5180	57.37	42.63

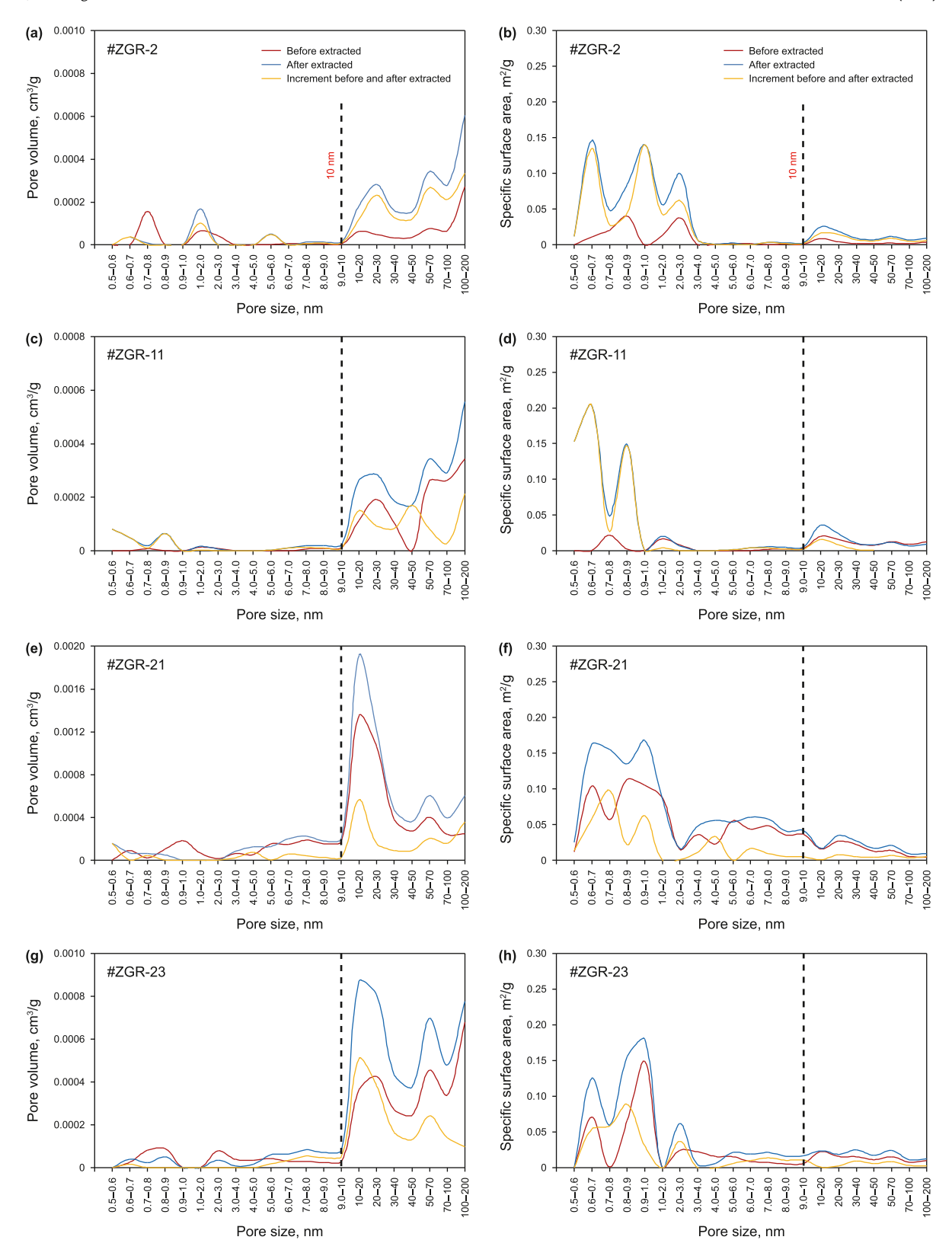


Fig. 9. Comparison of pore volume (a, c, e, g) and specific surface area (b, d, f, h) of typical samples before and after extraction (N<sub>2</sub> adsorption is mainly to obtain the distribution of mesopores and macropores, CO<sub>2</sub> adsorption is mainly to obtain the distribution of micropores).

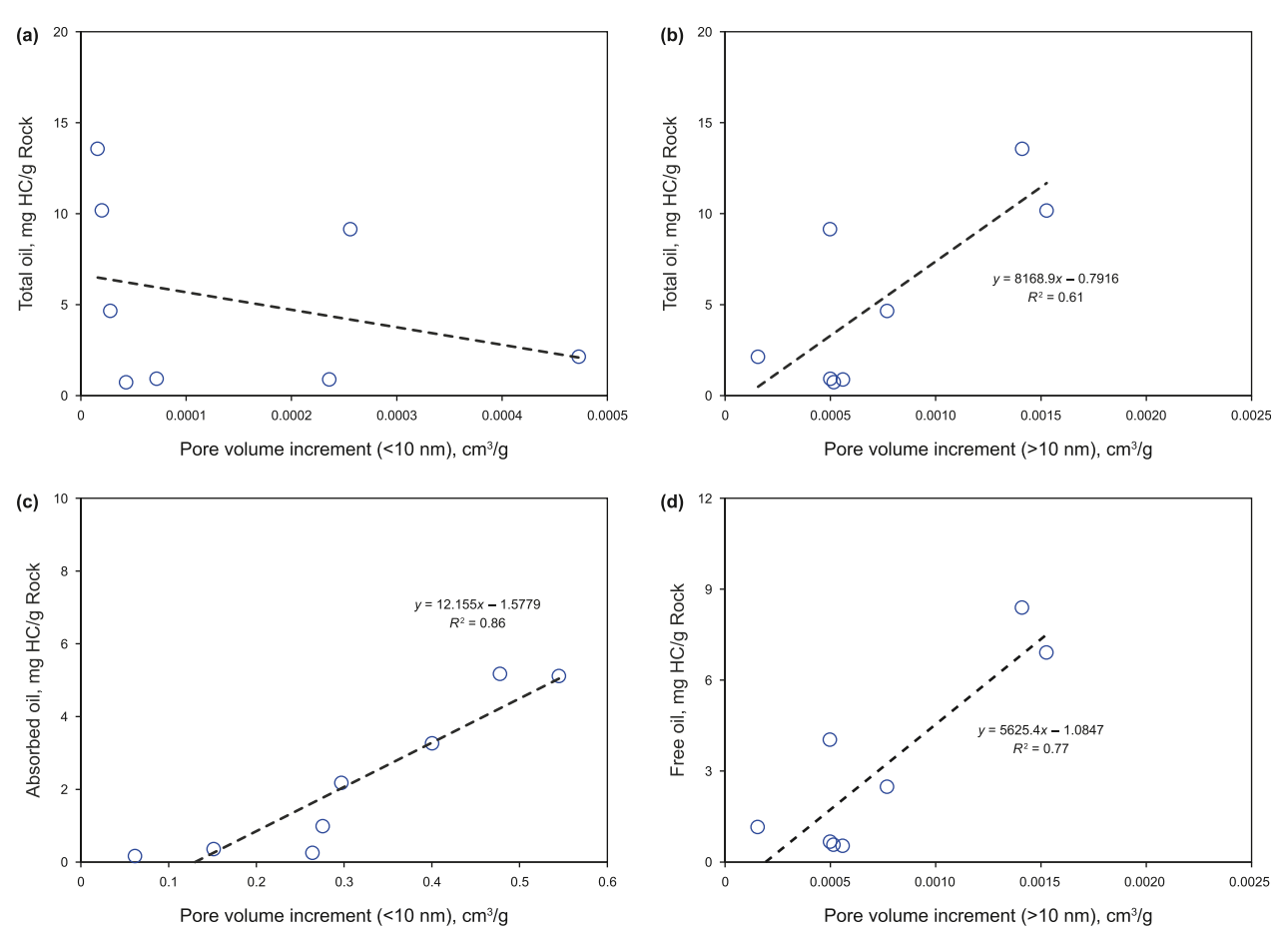


Fig. 10. The relationship between changes in pore structure at different scales and the shale oil content in various occurrence states before and after extraction.

 $10\,$  nm showed a positive correlation with free oil content (Fig. 10(d)), and the correlation was better than the correlation between the increment of pore volume with a diameter greater than  $10\,$  nm and total oil content. It is further shown that the adsorbed oil content is mainly controlled by the pore volume and specific surface area in the pore diameter less than  $10\,$  nm, while the free oil content is closely related to the pore volume in the pore diameter greater than  $10\,$  nm. Therefore, the retained shale oil mainly occurs in dominant pores with a diameter larger than  $10\,$  nm in a free state.

#### 4.4.2. Occurrence states

Scanning electron microscopy (SEM) and energy dispersive spectrum (EDS) shows the presence of oil and gas in the P<sub>1</sub>f. Shale oil predominantly exists within the shale layer in both free and adsorbed states. Adsorbed oil primarily exists on the surface of organic pores, clay mineral intercrystalline pores, and pyrite intercrystalline pores, appearing as thin films or flocculent strips, with blurred mineral boundaries (Fig. 11(a)-(d)). Free oil mainly occupies inorganic pores and microfractures with large pore sizes, often coated by mineral matrix in film form or disseminated form in intergranular pores and mineral particle solution pores (Fig. 11(e)–(g)). The color of the oil film and oil droplets is carbon black, in contrast to the color of the surrounding matrix, and the energy spectrum analysis of these oil droplets and oil film shows that the carbon peak characteristics are obvious and the organic composition is high (Fig. 11(h)). Furthermore, retained shale oil is observable in microfractures (Fig. 11(i)), suggesting that the effective combination of porosity and fractures formed by microfracture

communication serves as a favorable reservoir and migration pathway for shale oil. It is noteworthy that while shale oil can be observed in all types of pores in  $P_1f$  shale during the oil-generating stage, not all pores develop shale oil due to connectivity issues.

Two-dimensional nuclear magnetic resonance technology, as an effective method to indicate the microscopic occurrence state of pore fluids, has been widely used in the study of the occurrence mechanism of shale oil (Fleury and Romero-Sarmiento, 2016; Li et al., 2020; Mukhametdinova et al., 2021; Jiang et al., 2023; Zhang et al., 2023). According to the two-dimensional nuclear magnetic T<sub>1</sub>-T<sub>2</sub> map of hydrocarbon occurrence in P<sub>1</sub>f shale (Zhang et al., 2023), the distribution characteristics of T<sub>1</sub>-T<sub>2</sub> spectra of different lithofacies were compared. The results show that the signal distribution characteristics of different fluids in the NMR T<sub>1</sub>-T<sub>2</sub> spectrum of P<sub>1</sub>f shale are mainly controlled by the clay mineral content and the pyrolysis  $S_1$  value. The higher the clay mineral content, the stronger the water signal represented by zone 5, the larger the pyrolysis S<sub>1</sub> value, and the stronger the oil signal represented by zone 1. Taking ZGR-3 and ZGR-24 as examples, ZGR-3 is a felsic shale with high pyrolysis  $S_1$  (6.91 mg/g) and low clay mineral (6%), and the free oil signal is particularly strong on the NMR T<sub>1</sub>-T<sub>2</sub> spectrum, resulting in almost no signal in the bound water and structural water region, which is mainly free oil. ZGR-24 is a mixed shale with the highest clay mineral (31.1%) and low pyrolysis  $S_1$ (0.35 mg/g). On the NMR T<sub>1</sub>-T<sub>2</sub> spectrum, the signals in the bound water and structural water regions are dominant, while the signals in the free oil region are extremely weak. In particular, the NMR T<sub>1</sub>-T<sub>2</sub> spectra of different lithofacies differ greatly, but the NMR T<sub>1</sub>-T<sub>2</sub> spectra of the same lithofacies shale are similar. Felsic shale is

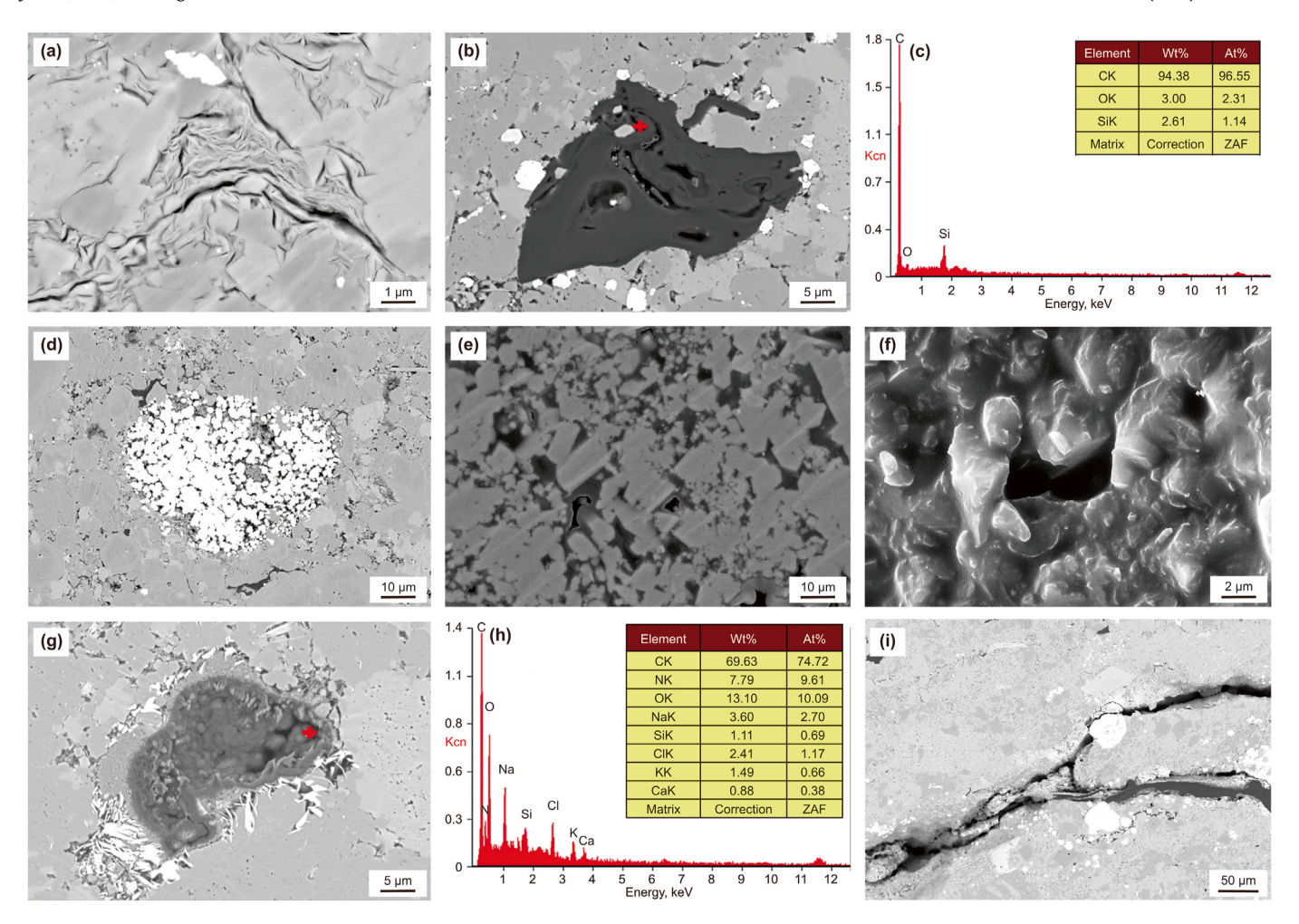


**Fig. 11.** Shale oil occurrence characteristics of P<sub>1</sub>f under SEM. (a) Oil film associated with clay mineral intercrystalline pores, MY1, 4605.54 m. (b) Floc oil occurrence inside organic pores, MY1, 4594.63 m. (c) EDS analysis of Red Cross points in (b). (d) Oil occurrence associated with pyrite intercrystalline pores, FN3, 4147.5 m. (e) Oil disseminated in intergranular pores, MY1, 4910.63 m. (f) Oil immersion in matrix and intergranular pores, MY1, 4812.58 m. (g) Carbonate mineral solution pores and oil droplets, FN3, 3955.58 m. (h) EDS analysis of Red Cross marks in (g). (i) Microcracks, FN1, 4362.88 m.

dominated by oil signals, showing strong free oil signals, and is mainly mobile oil in macropores (Fig. 12(a) and (b)). The fluid types of dolomitic shale and lime shale are complex, relatively speaking, the oil signal is stronger than the water signal, which contains both free oil and adsorbed oil, and the signal strength of free oil and adsorbed oil is roughly equal, showing a 1:1 ratio (Fig. 12(c)—(f)). The signals of free water, bound water, and structural water in mixed shale are extremely strong, and the oil signals are mainly adsorbed oil (Fig. 12(g) and (h)).

#### 4.5. Shale oil content in different occurrence states

The quantitative assessment of shale oil in different occurrence states holds significant importance for understanding the occurrence mechanism of oil and gas and assessing oil content. Currently, solvent extraction and pyrolysis methods are commonly employed to quantitatively characterize the physical state and quantity of shale oil, a topic extensively investigated by previous researchers (Jarvie, 2012; Li et al., 2018; Guan et al., 2022; Xu et al., 2022). The two-step pyrolysis method proposed by Li et al. (2018) is a new numerical method based on the traditional pyrolysis method. In this method, Total oil content =  $S_{1 \text{original}} + S_{2 \text{original}} - S_{2 \text{extraction}}$ , adsorbed oil =  $S_{2 \text{original}} - S_{2 \text{extraction}}$ , naturally,

free oil = total oil - adsorbed oil. The multi-step pyrolysis method proposed by Jiang et al. (2016) represents a significant advancement over traditional pyrolysis techniques. The combined content of  $S_{1-1}$ and  $S_{1-2}$  serves as an indicator of the free oil content in shale.  $S_{2-1}$ predominantly reflects adsorbed oil, and the total shale oil content can be determined by summing  $S_{1-1}$ ,  $S_{1-2}$ , and  $S_{2-1}$ . The hydrocarbon generation potential obtained by multi-step pyrolysis ( $S_{1-1}+S_{1-2}+S_{2-1}$  $_1+S_{2-2}$ ) showed a good positive correlation with conventional pyrolysis  $(S_1+S_2)$ , and the hydrocarbon generation potential obtained by multi-step pyrolysis experiment was greater than that obtained by conventional pyrolysis (Fig. 13(a)). In addition, the total oil content obtained by multi-step pyrolysis is significantly higher than that obtained by conventional pyrolysis. In this study, two different methods were employed to calculate the oil content of P<sub>1</sub>f shale in various occurrence states. Comparison of the total oil content, free oil content, and adsorbed oil content obtained using these methods revealed a strong positive correlation (Fig. 13(b)-(d)), indicating consistent trends in hydrocarbon content between two-step pyrolysis and multi-step pyrolysis. However, the total oil content and adsorbed oil content derived from two-step pyrolysis were higher than those from multi-step pyrolysis, while the free oil content from two-step pyrolysis was lower than that from multi-step pyrolysis. The discrepancy between the two methods lies in the determination

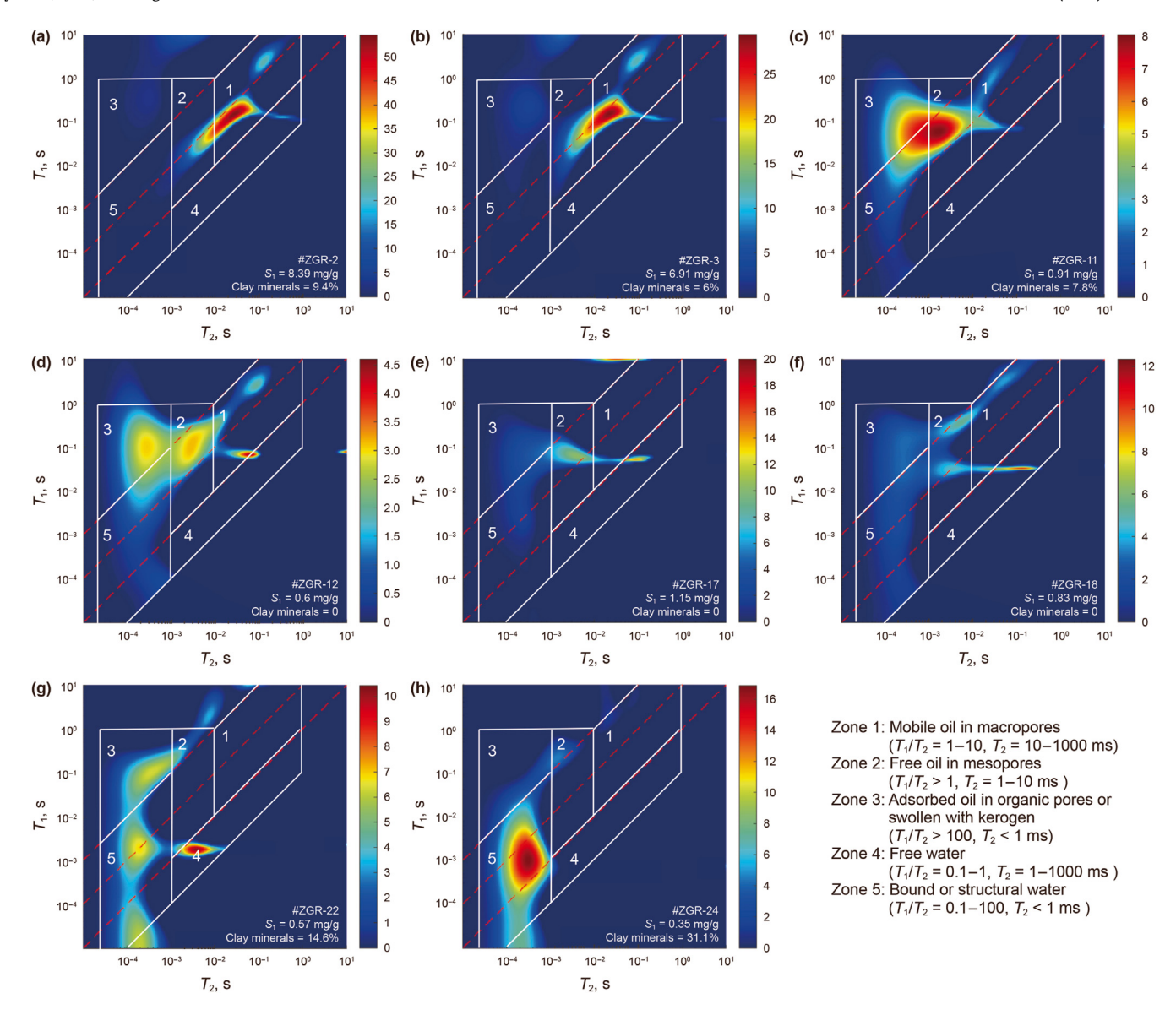


Fig. 12. Distribution characteristics of NMR  $T_1$ - $T_2$  in the original state of  $P_1f$ .

of free oil content. In multi-step pyrolysis, the free oil  $(S_{1-1}+S_{1-2})$  represents hydrocarbon products before 350 °C, while in two-step pyrolysis, the free oil  $(S_1)$  indicates the hydrocarbon content measured before 300 °C. It is evident that the hydrocarbons produced between 300 and 350 °C account for the differing calculation results between the two methods. Previous research has demonstrated that hydrocarbons generated at 300–350 °C consist mainly of high molecular weight (>C<sub>25</sub>) hydrocarbons, which exhibit limited mobility and should not be categorized as free oils (Jiang et al., 2016; Abrams et al., 2017; Guan et al., 2022). Consequently, the results from two-step pyrolysis are utilized in this study for the quantitative evaluation of shale oil in different occurrence states.

The shale oil content of  $P_1f$  shale in different occurrence states of Mahu sag is shown in Fig. 14. The total oil content of  $P_1f$  shale is large, ranging from 0.39 to 13.56 mg HC/g Rock, with an average of 3.19 mg HC/g Rock. The free oil content ranges from 0.35 to 8.39 mg HC/g Rock, with an average of 1.68 mg HC/g Rock. The adsorbed oil content ranges from 0.04 to 5.17 mg HC/g Rock, with an average value of 1.5 mg HC/g Rock. Additionally, variations in oil content exist among different lithofacies. Felsic shale exhibits the highest

total oil content, which is almost twice that of the other three lithofacies, and the total oil content is mainly free oil. Lime shale and dolomitic shale exhibit low total oil content, with a free oil to adsorbed oil ratio of 1:1. Mixed shale exhibits the highest adsorbed oil content among all lithofacies, with adsorbed oil comprising the main component of its total oil content. This is consistent with the occurrence characteristics of shale oil with different lithofacies observed in NMR  $T_1$ - $T_2$  spectra. It can be seen that the total oil content of felsic shale in  $P_1$ f of Mahu Sag is the highest, predominantly composed of free oil, indicating significant shale oil resource potential.

#### 4.6. Controlling factors of the oil occurrence

The shale rock skeleton is complex and changeable, and a three-phase complex with strong heterogeneity is formed after certain organic matter is contained. Shale oil is a kind of unconventional oil and gas formed by retention and accumulation in the original location of the shale reservoir (Jarvie, 2012; Zhu et al., 2019; Wu et al., 2022). The enrichment of shale oil depends on the complex

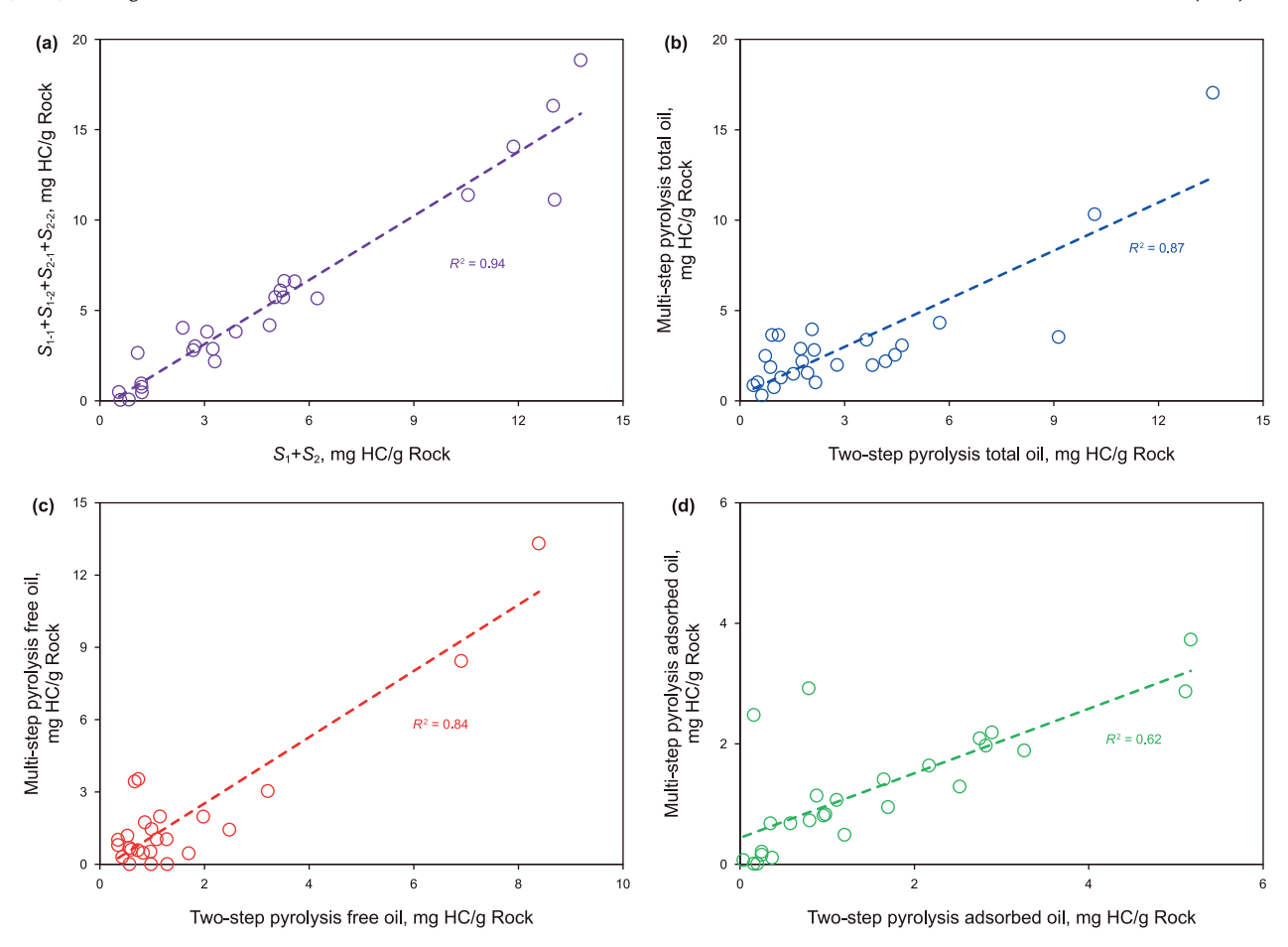


Fig. 13. Comparison of results of two-step pyrolysis and multi-step pyrolysis.

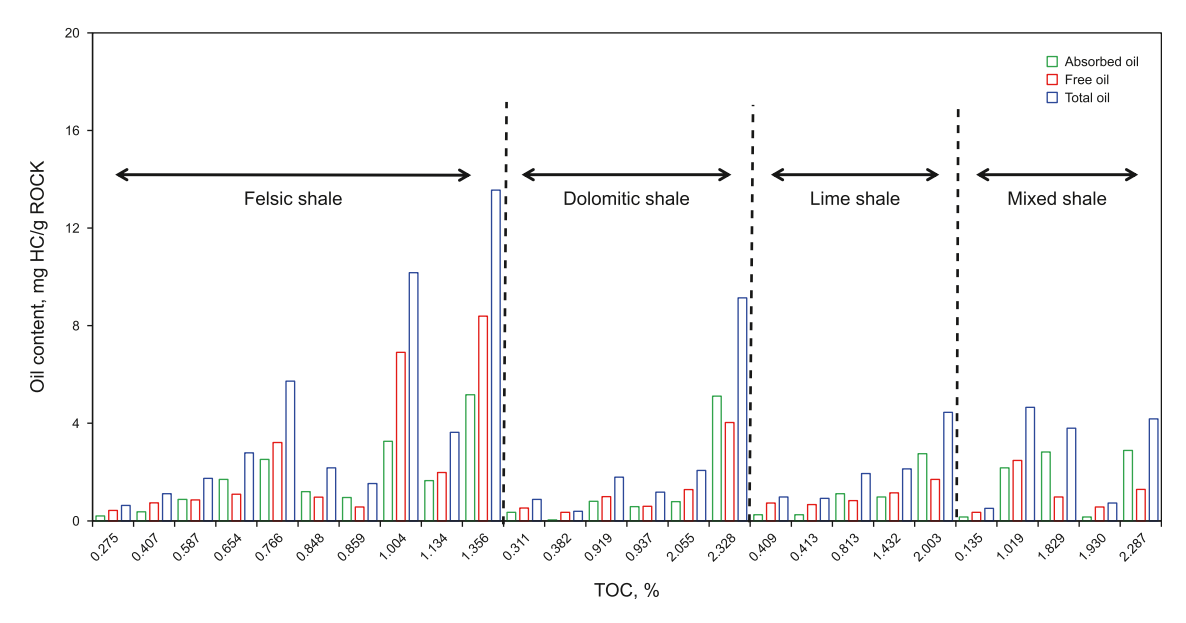


Fig. 14. Distribution of oil content in different lithofacies.

shale oil system, and the occurrence characteristics of shale oil are controlled by the inorganic components, organic components, and pore skeleton patterns that constitute the shale oil system (Han et al., 2015; Shao et al., 2018; Wang et al., 2019; Zhang et al., 2021; Guan et al., 2022; Wu et al., 2022; Hu et al., 2025).

# 4.6.1. Organic matter

Organic matter is the main medium for shale oil adsorption, and the characteristics of organic matter are the key factors affecting the occurrence of shale oil and gas (Salama et al., 2021; Wu et al., 2022; Lv et al., 2023). Fig. 14 shows the occurrence characteristics

of shale oil in different lithofacies with different abundance of organic matter, indicating that mechanical abundance has a complex control effect on oil distribution in pores through hydrocarbon generation and adsorption capacity. Lu et al. (2012) proposed the "three-part method" to conduct a classification evaluation of shale oil resources. With the increase of TOC, free oil content gradually increases in three stages (Fig. 15(a)). When TOC < 0.2%, free oil increases slowly. When 0.2% < TOC < 0.8%, the free oil increases rapidly, and when TOC > 0.8%, the free oil enters the plateau. At the same time, the adsorbed oil content showed a positive correlation with TOC (Fig. 15(b)), and the adsorbed oil content increased with the increase of TOC. However, the positive correlation between adsorbed oil content and TOC in the mixed shale is weak, which may be caused by more clay minerals in the mixed shale, indicating that in the mixed shale, besides the dissolution of organic matter and adsorption on the surface of organic pores, the adsorption on the surface of clay minerals is particularly important. In addition, the type of kerogen also affects the occurrence and distribution of shale oil. As shown in Fig. 15(c), the content of shale oil varies among different types of kerogens. The better the kerogen type, the higher the retained hydrocarbon content in shale, among which the total oil content of type I-II<sub>1</sub> kerogen is 5 times that of type III kerogen. As can be seen from Fig. 15(d), the proportion of adsorbed oil gradually decreases with the increase of depth, indicating the controlling influence of thermal maturity on microscopic oil occurrence. With increasing depth and thermal maturity, liquid hydrocarbons generated from organic matter gradually become

lighter, while aliphatic chains, carboxyl, and hydroxyl groups in shale organic matter gradually diminish. This disparity between residual hydrocarbons within the shale and organic matter structure intensifies, leading to a weakening adsorption capacity of organic matter for residual hydrocarbons with increasing thermal maturity (Jiang et al., 2016; Shao et al., 2018; Zhu et al., 2019). Consequently, the proportion of adsorbed oil in shale decreases, while mobilizability increases.

#### 4.6.2. pore structure

Shale oil is formed by retention and accumulation in the original location of the shale reservoir, so shale pore structure is an important factor affecting the occurrence of shale oil (Nie et al., 2016; Li et al., 2017; Pan et al., 2019). As shown in Fig. 16(a) and (b), the total oil content of shale presents a positive correlation with porosity, and the proportion of adsorbed oil gradually decreases with the increase of the average pore diameter of shale. This shows that the shale reservoir quality determines the enrichment potential of shale oil, and the occurrence state of shale oil varies across pores of different scales and levels. During the process of shale hydrocarbon generation, strong adsorption occurs in the early stages, leading to oil primarily existing in the form of adsorbed oil. As the generated oil fulfills the adsorption requirements of kerogen and inorganic minerals, free oil emerges. Free oil is more likely to reside in larger pores compared to adsorbed oil. The results indicated a positive correlation between the content of free oil and the pore volume ratio of pores with a diameter larger than 10 nm, and

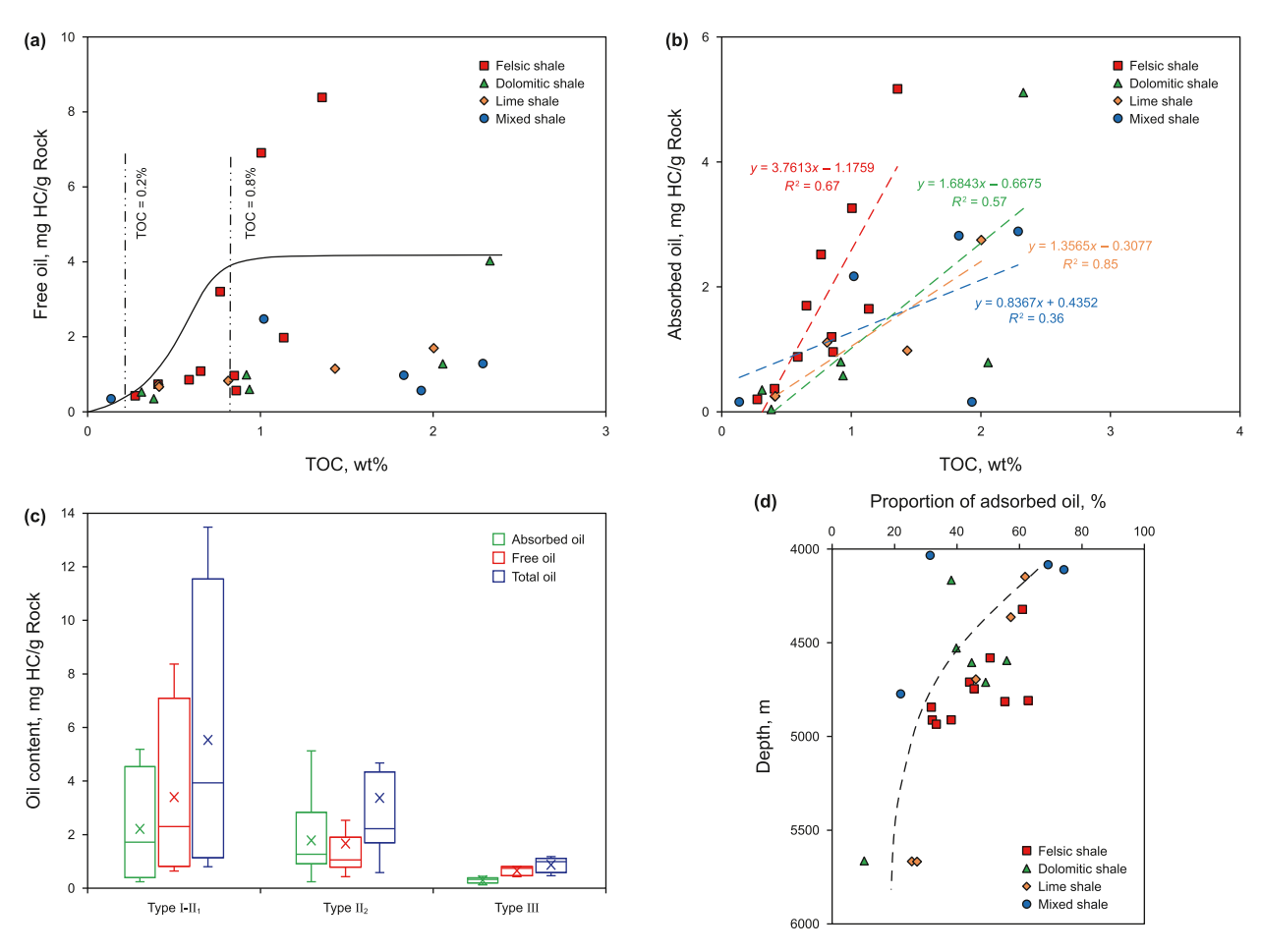


Fig. 15. The relationship between free oil content (a) and adsorbed oil content (b) and TOC; (c) Occurrence characteristics of shale oil of different kerogen types; (d) Relationship between the proportion of adsorbed oil and depth.

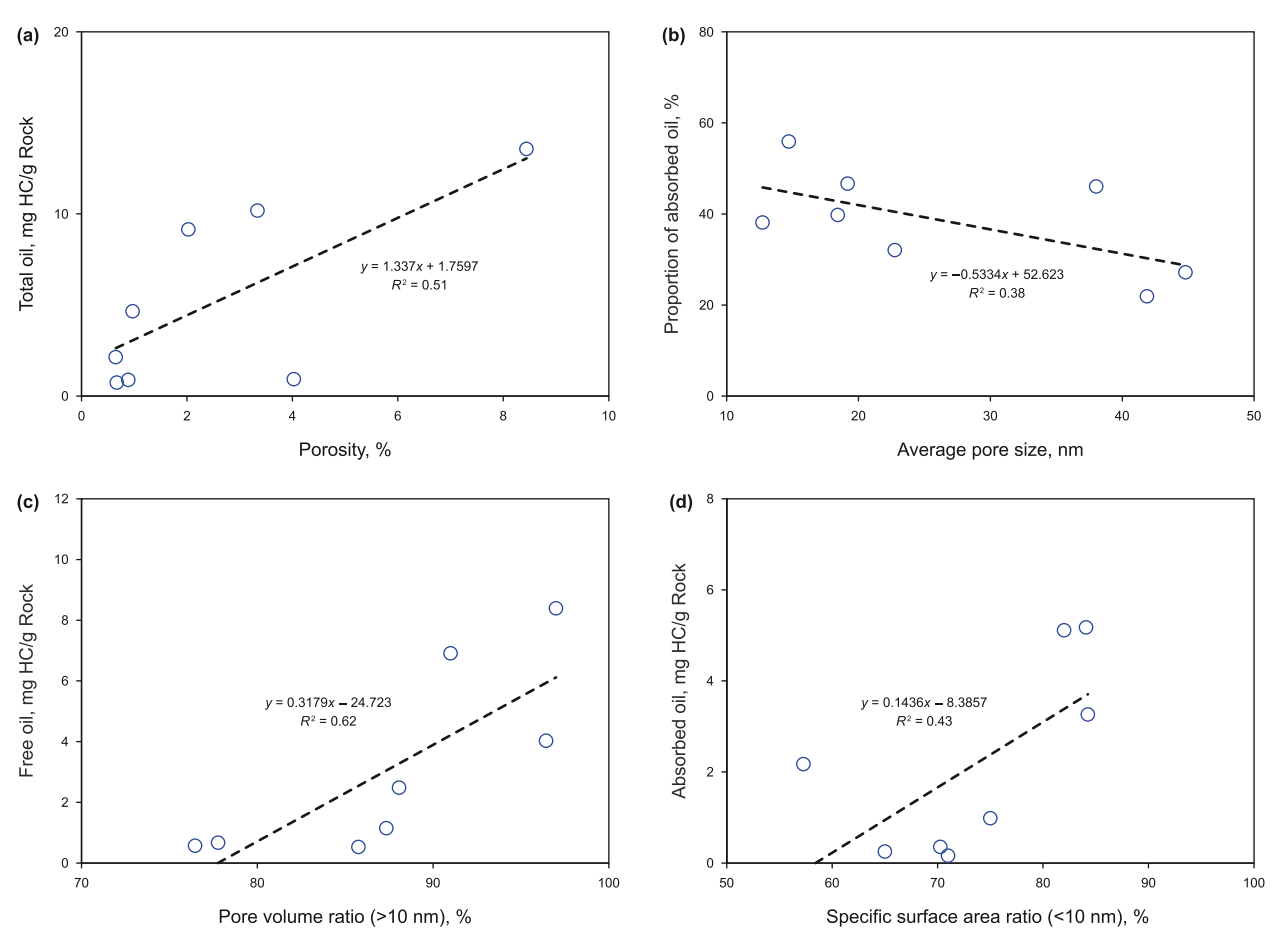


Fig. 16. Relationship between oil content and pore structure parameters in P<sub>1</sub>f.

between the content of adsorbed oil and the specific surface area ratio of pores with a diameter smaller than 10 nm (Fig. 16(c) and (d)), which further indicated that free oil was mainly controlled by large pores with a diameter larger than 10 nm, and adsorbed oil was mainly controlled by small pores with a diameter smaller than 10 nm. Large pores offer ample pore volume conducive to free oil enrichment, while small pores offer sufficient specific surface area for adsorbed oil accumulation.

#### 4.6.3. Mineral compositions

Different mineral compositions differ in the wettability of hydrocarbon substances, resulting in different adsorption capacities of different minerals and the occurrence of hydrocarbon components, which directly affect the occurrence characteristics of shale oil (Siddiqui et al., 2018; Guan et al., 2022). Lithofacies are the most direct reflection of different mineral compositions. Among all lithofacies, felsic shale has the highest free oil content, and mixed shale has the highest adsorbed oil content (Fig. 17(a)). Fig. 17(b) illustrates that free oil content increases with rising felsic mineral content. This is attributed to the enhanced reservoir space provided by increased felsic minerals, facilitating internal micro-migration within shale layers and the acceptance of free hydrocarbons from external layers, thus promoting free oil enrichment. Conversely, Fig. 17(c) and (d) indicates a decrease in free oil content with increasing clay mineral content. This aligns with the observation that mixed shale, rich in clay minerals, exhibits maximal adsorbed oil content. Clay minerals possess large specific surface areas and tend to undergo lipophilic transformation during diagenetic evolution, providing conducive reservoir space and adsorption sites for

adsorbed oil accumulation. Notably, Fig. 17(e) reveals no correlation between carbonate mineral proportion and adsorbed oil content, suggesting the complex influence of carbonate minerals on shale oil occurrence.

#### 4.7. Shale oil occurrence pattern

The occurrence mechanism of shale oil is the reflection of the interaction between shale oil and mud shale. First, the understanding of the occurrence characteristics of shale oil at the microscopic scale is the core issue, including the contribution of pore space to shale oil and the difference between microscopic oil occurrence in organic and inorganic minerals. Shale oil can exist in free, dissolved, and adsorbed states, with the P<sub>1</sub>f primarily containing shale oil in free and adsorbed states. Under SEM, it is found that the shale of P<sub>1</sub>f has a large number of micro and nanopores. The development characteristics of pores, fractures, and shale oil in 563 FE-SEM photos of 26 samples were statistically analyzed, and an occurrence pattern of shale oil in microscopic pores was initially established (Fig. 18). Since a large amount of movable oil and light hydrocarbons have been lost in the core at present, the pattern represents the microscopic occurrence of residual oil in the pores in the original formation state. Free oil exists in various dominant pores with pore size greater than 10 nm, mainly in large rigid mineral intergranular pores, dissolved pores and microfractures of carbonate minerals, and adsorbed oil is mainly adsorbed on the surface of organic matter and some clay minerals. The free water is distributed in some inorganic pores with large pore sizes, among which the interlayer pores associated with clay minerals are often

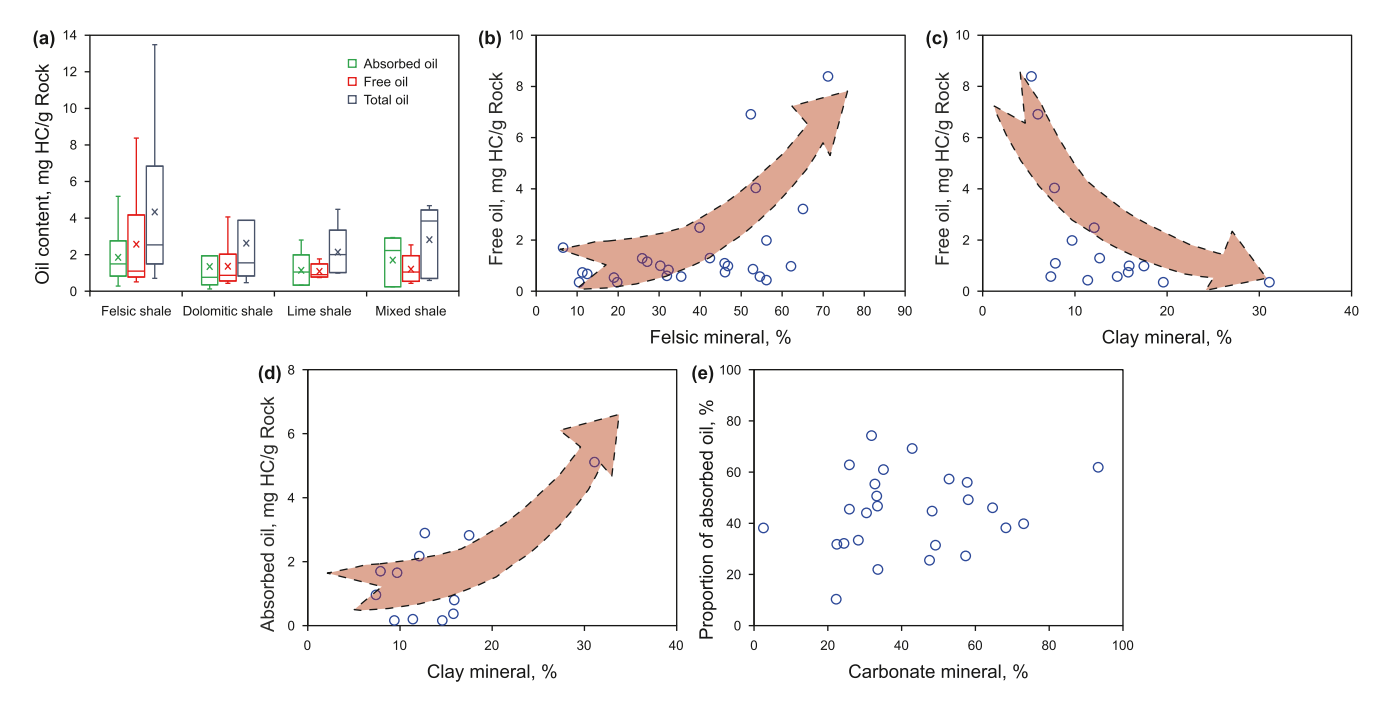


**Fig. 17.** (a) Comparison of oil content of shale with different lithofacies; Correlation of free oil content with felsic mineral (b) and clay mineral (c); (d) Correlation between adsorbed oil content and clay mineral content; (e) Correlation between adsorbed oil proportion and carbonate mineral content.

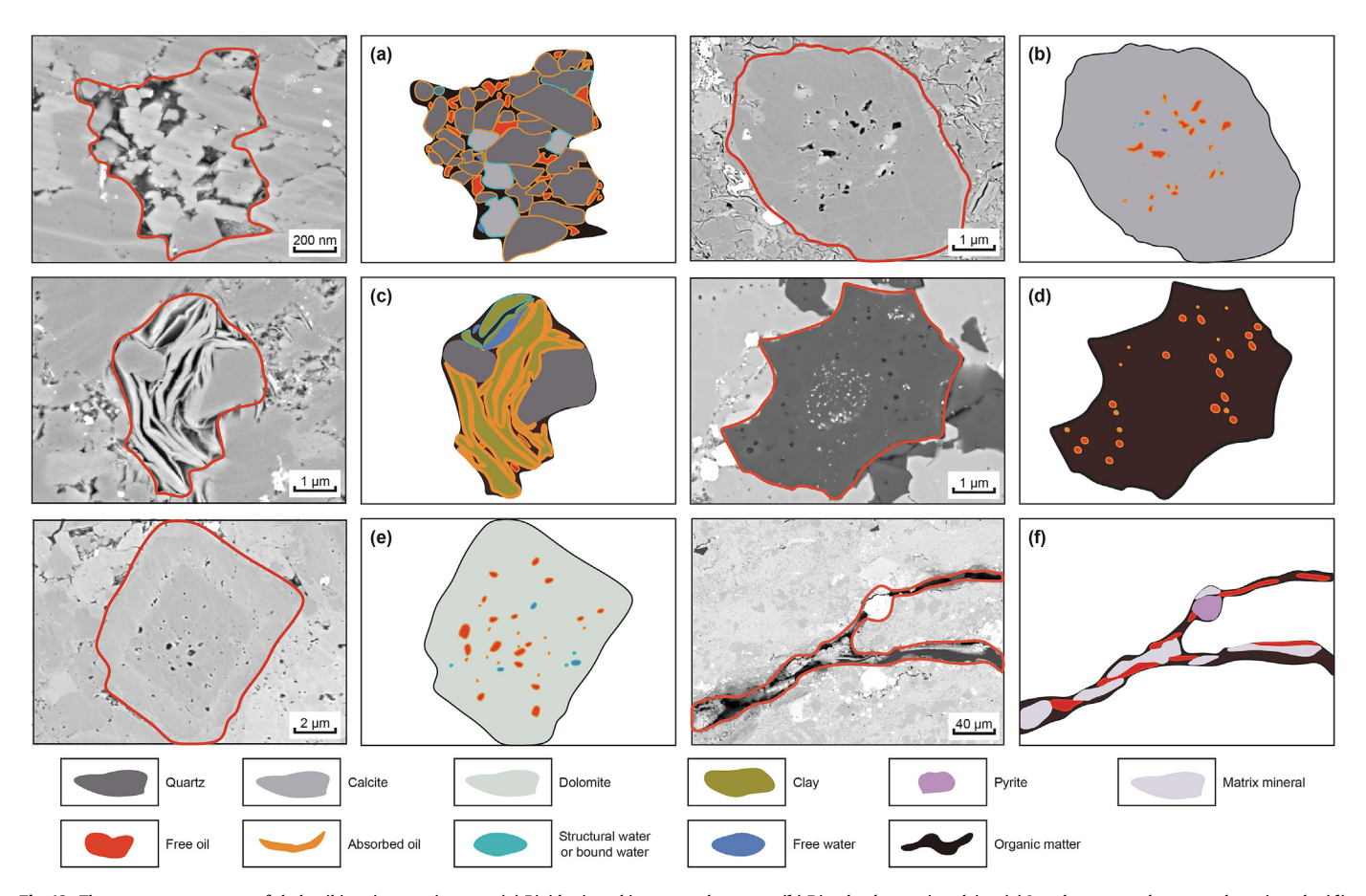


Fig. 18. The occurrence pattern of shale oil in microscopic pores. (a) Rigid mineral intergranular pores; (b) Dissolved pores in calcite; (c) Interlayer pores between clay minerals; (d) Organic pores; (e) Dissolved pores in dolomite; (f) Microfractures.

developed. Structural water and bound water mainly exist on the surface of clay minerals and around some inorganic pores. P<sub>1</sub>f shale, a representative alkaline lacustrine shale oil, differs markedly from freshwater lacustrine shale due to differences in sedimentary environment, rock fabric, organic matter composition, and hydrocarbon generation potential (Yu et al., 2018; Cao et al., 2020; Zhao et al., 2020; Tang et al., 2021). In alkaline lake basins, shale exhibits lower clay mineral content compared to freshwater lake basins, resulting in 35% less adsorption of inorganic minerals and reduced adsorption of liquid hydrocarbons (Li et al., 2016; Zhao et al., 2020, 2023). Moreover, higher brittle mineral content and the presence of free oil within shale contribute to a lower mobility threshold for shale oil in alkaline lake basins compared to freshwater lake basins, enhancing shale oil mobility. Nevertheless, the majority of alkaline lake basin shale in China exhibits low thermal maturity, high density, and viscosity of crude oil, along with low aromatic content, contributing to the complexity of shale oil occurrence characteristics in alkaline lake basins (Zou et al., 2019b; Yu et al., 2019).

The above research shows that the occurrence of shale oil depends on the complex shale oil system, and the occurrence characteristics of shale oil are controlled by the inorganic components, organic components, and pore skeleton patterns that constitute the shale oil system. Different lithofacies have different shale oil occurrence characteristics. Based on an occurrence pattern of shale oil in microscopic pores, to further reveal the occurrence mechanism and mobility of shale oil, we established shale oil occurrence patterns of different lithofacies (Fig. 19). Felsic shale exhibits a high abundance of dominant pores, possesses the highest oil content,

predominantly harbors free oil within these dominant pores, and demonstrates good mobility. Fluid occurrence in dolomitic shale and lime shale is intricate, with low oil content and a free oil to adsorbed oil ratio of 1:1. Mixed shale exhibits elevated clay mineral content and a scarcity of dominant pores. Moreover, ineffective pores contain increased bound water, resulting in medium oil content and limited mobility predominantly due to adsorption. Herein, during the exploration and development of alkaline lacustrine shale oil resources, emphasis should be placed on identifying sweet spots within the felsic shale characterized by dominant pores.

#### 5. Conclusions

The occurrence mechanism of shale oil in  $P_1f$  was investigated using a combination of geochemistry, Soxhlet extraction, field emission scanning electron microscopy, gas adsorption, and nuclear magnetic resonance  $T_1$ - $T_2$  spectroscopy.  $P_1f$  primarily consists of felsic shale, dolomitic shale, lime shale, and mixed shale. The shale in  $P_1f$  exhibits numerous micro and nanopores, with matrix pores and microfractures associated with inorganic minerals being the predominant types of pores. Although shale oil is observed in all types of pores during the oil-generating stage, not all pores contain shale oil. Shale oil mainly occurs in the shale layer in free and adsorbed states, with adsorbed oil predominantly located on the surface of organic matter and clay minerals, while free oil mainly resides in inorganic pores and microfractures with large pore sizes.

Shale oil accumulation varies across different scale levels of pores, with free oil and adsorbed oil predominantly controlled by

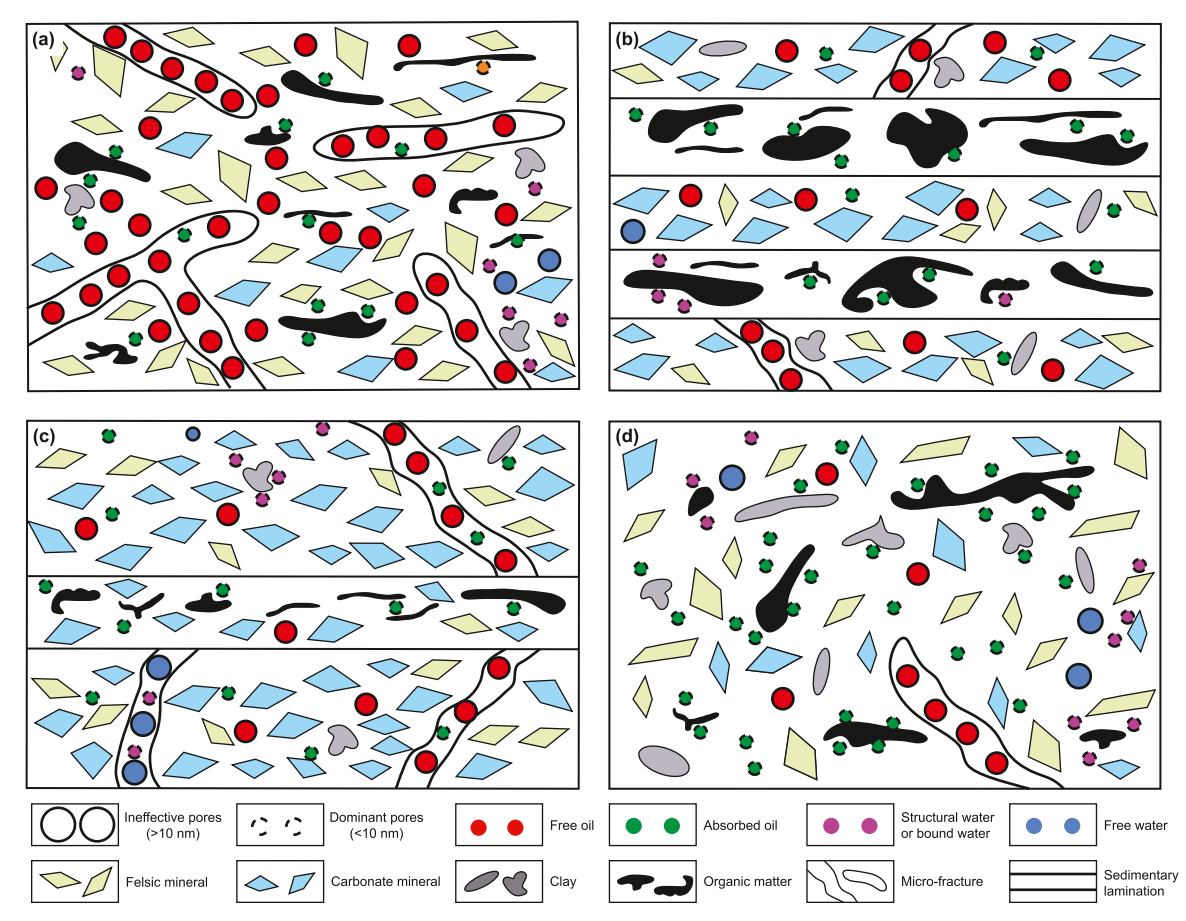


Fig. 19. Shale oil occurrence patterns of different lithofacies in the P<sub>1</sub>f of the Mahu Sag. (a) Felsic shale, (b) dolomitic shale, (c) lime shale, (d) mixed shale.

dominant pores with diameters exceeding 10 nm and ineffective pores with diameters less than 10 nm, respectively. Currently, retained shale oil primarily exists in free form within dominant pores with diameters larger than 10 nm. The occurrence characteristics of shale oil are intricately linked to organic matter, pore structure, and mineral composition. Organic matter exerts a complex control on oil distribution in pores through hydrocarbon generation and adsorption capacity. Shale reservoir quality dictates the enrichment potential of shale oil, with total oil content positively correlated with porosity. Furthermore, the proportion of adsorbed oil diminishes as the average pore diameter of shale increases. Additionally, elevated felsic mineral content promotes free oil enrichment, while increased clay mineral content facilitates adsorbed oil accumulation.

The total oil content of  $P_1f$  shale is large, ranging from 0.39 to 13.56 mg HC/g Rock, with an average value of 3.19 mg HC/g Rock. The dominant exploration area of shale oil resources coincides with the free oil enrichment area. The distribution of oil content varies significantly among different lithofacies. Felsic shale exhibits the highest total oil content, predominantly comprising free oil. Lime shale and dolomitic shale possess relatively low total oil content, with a free-to-adsorbed oil ratio of 1:1. Mixed shale primarily contains adsorbed oil. Additionally, based on the microscopic pore occurrence pattern of shale oil, we delineated shale oil occurrence patterns across various lithofacies. To conclude, in the exploration and development of alkaline lacustrine shale oil resources, emphasis should be placed on identifying sweet spots within felsic shale featuring dominant pores.

#### **CRediT authorship contribution statement**

Jia-Hao Lv: Writing — review & editing, Writing — original draft, Visualization, Validation, Supervision, Methodology, Investigation, Formal analysis, Data curation, Conceptualization. Tao Hu: Supervision, Resources, Project administration, Methodology, Funding acquisition, Conceptualization. Wang Zhang: Supervision, Resources, Project administration, Funding acquisition, Conceptualization. Fu-Jie Jiang: Supervision, Resources, Project administration, Methodology, Funding acquisition. Jing Xue: Visualization, Validation, Software, Investigation, Data curation. Chen-Xi Zhang: Writing — original draft, Visualization, Software, Methodology, Investigation. Zhen-Guo Qi: Writing — review & editing, Writing — original draft, Software, Investigation, Data curation. Ren-Da Huang: Writing — original draft, Visualization, Validation, Software. Mei-Ling Hu: Writing — review & editing, Visualization, Validation. Shu Jiang: Project administration, Resources, Supervision.

#### **Declaration of competing interest**

The authors declare that they have no known competing financial interests or personal relationships that could have appeared to influence the work reported in this paper.

#### Acknowledgments

This study was financially supported by the State Key Laboratory of Shale Oil and Gas Enrichment Mechanisms and Efficient Development (33550000-22-ZC0613-0006), National Natural Science Foundation of China (42202133), CNPC Innovation Fund (2022DQ02-0106), Strategic Cooperation Technology Projects of the CNPC and CUPB (ZLZX2020-01-05), Key Laboratory of Tectonics and Petroleum Resources (China University of Geosciences), Ministry of Education, China (TPR-2023-05). We thank Xinjiang Oilfield Company for providing samples and background geological data in this study.

#### References

- Abrams, M.A., Gong, C., Garnier, C., Sephton, M.A., 2017. A new thermal extraction protocol to evaluate liquid-rich unconventional oil in place and in-situ fluid chemistry. Mar. Petrol. Geol. 88, 659–675. https://doi.org/10.1016/j.marpetgeo.2017.09.014.
- Akkutlu, I.Y., Baek, S., Olorode, O.M., Wei, P., Zhang, T., Shuang, A., 2017. Shale resource assessment in presence of nanopore Confinement, URTEC-2670808-MS. In: Unconventional Resources Technology Conference, SPE/AAPC/SEG Unconventional Resources Technology Conference. https://doi.org/10.15530/URTEC-2017-2670808.
- Cao, J., Lei, D., Li, Y., Tang, Y., A, B.L.M.T., Chang, Q., Wang, T., 2015. High quality source rock from ancient Alkali Lake: lower Permian Fengcheng Formation, lunggar Basin. Acta Pet. Sin. 36 (7), 781–790 (in Chinese).
- Junggar Basin. Acta Pet. Sin. 36 (7), 781–790 (in Chinese).

  Cao, J., Xia, L., Wang, T., Zhi, D., Tang, Y., Li, W., 2020. An alkaline lake in the Late Paleozoic Ice Age (LPIA): a review and new insights into paleo environment and petroleum geology. Earth Sci. Rev. 202, 103091. https://doi.org/10.1016/j.earscirev.2020.103091.
- Cui, J., Cheng, L., 2017. A theoretical study of the occurrence state of shale oil based on the pore sizes of mixed Gaussian distribution. Fuel 206, 564–571. https:// doi.org/10.1016/i.fuel.2017.06.047.
- Dembicki, H.J., Horsfield, B., Ho, T.T.Y., 1983. Source rock evaluation by pyrolysis-gas chromatography. AAPG Bull. 67 (7), 1094–1103. https://doi.org/10.1306/03B5B709-16D1-11D7-8645000102C1865D.
- Feng, C., Li, T., He, W., Zheng, M., 2020. Organic geochemical traits and paleo-depositional conditions of source rocks from the Carboniferous to Permian sediments of the Northern Mahu Sag, Junggar Basin, China. J. Petrol. Sci. Eng. 191, 107–117. https://doi.org/10.1016/j.petrol.2020.107117.
- Fleury, M., Romero-Sarmiento, M., 2016. Characterization of shales using T<sub>1</sub>-T<sub>2</sub> NMR maps. J. Petrol. Sci. Eng. 137, 55–60. https://doi.org/10.1016/j.petrol.2015.11.006.
- Guan, M., Liu, X., Jin, Z., Lai, J., Liu, J., Sun, B., Liu, T., Hua, Z., Xu, W., Shu, H., Wang, G., Liu, M., Luo, Y., 2022. Quantitative characterization of various oil contents and spatial distribution in lacustrine shales: insight from petroleum compositional characteristics derived from programmed pyrolysis. Mar. Petrol. Geol. 138, 105522. https://doi.org/10.1016/j.marpetgeo.2021.105522.
- Guo, P., Wen, H., Gibert, L., Jin, J., Wang, J., Lei, H., 2021. Deposition and diagenesis of the Early Permian volcanic-related alkaline playa-lake dolomitic shales, NW Junggar Basin, NW China. Mar. Petrol. Geol. 123, 104780. https://doi.org/10.1016/ j.marpetgeo.2020.104780.
- Guo, Q., Yao, Y., Hou, L., Tang, S., Pan, S., Yang, F., 2022. Oil migration, retention, and differential accumulation in "sandwiched" lacustrine shale oil systems from the Chang 7 member of the Upper Triassic Yanchang Formation, Ordos Basin, China. Int. J. Coal Geol. 261, 104077. https://doi.org/10.1016/j.coal.2022.104077.
- Han, Y., Mahlstedt, N., Horsfield, B., 2015. The Barnett Shale: compositional fractionation associated with intraformational petroleum migration, retention and expulsion. AAPG (Am. Assoc. Pet. Geol.) Bull. 99, 2173–2202. https://doi.org/10.1306/06231514113.
- Hu, T., Pang, X., Jiang, S., Wang, Q., Li, H., 2018. Oil content evaluation of lacustrine organic-rich shale with strong heterogeneity: a case study of the Middle Permian Lucaogou Formation in Jimusaer Sag, Junggar Basin, NW China. Fuel 221, 196–205. https://doi.org/10.1016/j.fuel.2018.02.082.
- Hu, T., Pang, X., Jiang, F., Wang, Q., Wu, G., Liu, X., Jiang, S., Li, C., Xu, T., Chen, Y., 2021. Key factors controlling shale oil enrichment in saline lacustrine rift basin: implications from two shale oil wells in Dongpu Depression, Bohai Bay Basin. Petrol. Sci. 18, 687–711. https://doi.org/10.1007/s12182-021-00564-z.
- Hu, T., Liu, Y., Jiang, F., Pang, X., Wang, Q., Zhou, K., Wu, G., Jiang, Z., Huang, L., Jiang, S., Zhang, C., Li, M., Chen, Z., 2024a. A novel method for quantifying hydrocarbon micromigration in heterogeneous shale and the controlling mechanism. Energy 288, 129712. https://doi.org/10.1016/j.energy.2023.129712.
- Hu, T., Jiang, F., Pang, X., Liu, Y., Wu, G., Zhou, K., Xiao, H., Jiang, Z., Li, M., Jiang, S., Huang, L., Chen, D., Meng, Q., 2024b. Identification and evaluation of shale oil micro-migration and its petroleum geological significance. Petrol. Explore. Dev. 51 (1), 127–140. https://doi.org/10.1016/S1876-3804(24)60010-8.
- Hu, T., Jing, Z., Zhang, Q., Pan, Y., Yuan, M., Li, M., 2025. Shale oil micro-migration characterization: key methods and outlook. Advances in Geo-Energy Research 15 (1), 5–12. https://doi.org/10.46690/ager.2025.01.02.
- Jarvie, D.M., 2012. Shale resource systems for oil and gas: Part 2—Shale oil resource systems. In: Breyer, J.A. (Ed.), Shale Reservoirs—Giant Resources for the 21st Century, vol. 97. Am. Assoc. Pet. Geol. Bull., pp. 89—119. https://doi.org/10.1306/ 13321447M973489
- Jarvie, D.M., Hill, R.J., Ruble, T.E., Pollastro, R.M., 2007. Unconventional shale-gas systems: the Mississippian Barnett Shale of north-central Texas as one model forther mogenic shale gas assessment. Am. Assoc. Petrol. Geol. Bull. 91, 475–499. https://doi.org/10.1306/12190606068.
- Jiang, C., Wang, G., Song, L., Huang, L., Wang, S., 2023. Identification of fluid types and their implications for petroleum exploration in the shale oil reservoir: a case study of the Fengcheng Formation in the Mahu Sag, Junggar Basin, Northwest China. Mar. Petrol. Geol. 147, 105996. https://doi.org/10.1016/ j.marpetgeo.2022.105996.
- Jiang, Q., Li, M., Qian, M., Qian, M., Li, Z., Li, Z., Huang, Z., 2016. Quantitative characterization of shale oil in different occurrence states and its application. Petrol. Geol. Exp. 38 (6), 842–849. https://doi.org/10.11781/sysydz201606842 (in Chinese).
- Jin, Z., Liang, X., Bai, Z., 2022. Exploration breakthrough and its significance of

Gulong lacustrine shale oil in the Songliao Basin, Northeastern China. Energy Geosci 3, 120–125. https://doi.org/10.1016/j.engeos.2022.01.005.

- Katz, B.J., Lin, F., 2021. Consideration of the limitations of thermal maturity with respect to vitrinite reflectance, Tmax, and other proxies. AAPG (Am. Assoc. Pet. Geol.) Bull. 105, 695—720. https://doi.org/10.1306/09242019261.
- Kausik, R., Fellah, K., Feng, L., Freed, D., Simpson, G., 2016. High- and Low-Field NMR relaxometry and diffusometry of the bakken petroleum system. In: SPWLA 57th Annual Logging Symposium.
- Li, J., Jiang, C., Wang, M., Lu, S., Chen, Z., Chen, G., Li, J., Li, Z., Lu, S., 2020. Adsorbed and free hydrocarbons in unconventional shale reservoir: a new insight from NMR T<sub>1</sub>-T<sub>2</sub> maps. Mar. Petrol. Geol. 116, 104311. https://doi.org/10.1016/ i.marpetgeo.2020.104311.
- Li, M., Chen, Z., Ma, X., Cao, T., Li, Z., Jiang, Q., 2018. A numerical method for calculating total oil yield using a single routine Rock-Eval program: a case study of the Eocene Shahejie Formation in Dongying Depression, Bohai Bay Basin, China. Int. J. Coal Geol. 191, 49–65. https://doi.org/10.1016/j.coal.2018.03.004.
- Li, T., Jiang, Z., Xu, C., Liu, B., Liu, G., Wang, P., Li, X., Chen, W., Ning, C., Wang, Z., 2017. Effect of pore structure on shale oil accumulation in the lower third member of the Shahejie formation, Zhanhua Sag, eastern China: Evidence from gas adsorption and nuclear magnetic resonance. Mar. Petrol. Geol. 88, 932—949. https://doi.org/10.1016/j.marpetgeo.2017.09.030.
- Li, W., Cao, J., Zhi, D., Tang, Y., He, W., Wang, T., Xia, L., 2021. Controls on shale oil accumulation in alkaline lacustrine settings: Late Paleozoic Fengcheng Formation, northwestern Junggar Basin. Mar. Petrol. Geol. 129, 105107. https://doi.org/10.1016/j.marpetseo.2021.105107.
- 10.1016/j.marpetgeo.2021.105107.
  Li, W., Lu, S., Xue, H., Zhang, P., Wu, S., 2015. The formation environment and developmental models of argillaceous dolomite in the Xingouzui Formation, the Jianghan Basin. Mar. Petrol. Geol. 67, 692–700. https://doi.org/10.1016/j.marpetgeo.2015.06.011.
- Li, Z., Zou, Y., Xu, X., Sun, J., Li, M., Peng, P., 2016. Adsorption of mudstone source rock for shale oil experiments, model and a case study. Org. Geochem. 92, 55–62. https://doi.org/10.1016/j.orggeochem.2015.12.009.
- Liu, C., Xingyou, X., Liu, K., Jing, B., Lin, W., Chen, S., 2020. Pore-scale oil distribution in shales of the Qingshankou Formation in the Changling sag, Songliao Basin, NE China. Mar. Petrol. Geol. 120, 104553. https://doi.org/10.1016/ j.marpetgeo.2020.104553.
- Liu, G., Chen, Z., Wang, X., Gao, G., Xiang, B., Ren, J., Ma, W., 2016. Migration and accumulation of crude oils from Permian lacustrine source rocks to Triassic reservoirs in the Mahu depression of Junggar Basin, NW China: constraints from pyrrolic nitrogen compounds and fluid inclusion analysis. Org. Geochem. 101, 82–98. https://doi.org/10.1016/j.orggeochem.2016.08.013.
- Liu, K., Ostadhassan, M., Zhou, J., Gentizs, T., Rezaee, R., 2017. Nanoscale pore structure characterization of the bakken shale in the USA. Fuel 209, 567–578. https://doi.org/10.1016/j.fuel.2017.08.034.
- Lu, S., Huang, W., Chen, F., Li, J., Wang, M., Xue, H., Wang, W., Cai, X., 2012. Classification and evaluation criteria of shale oil and gas resources: discussion and application. Petrol. Explore. Dev. 39, 268–276. https://doi.org/10.1016/S1876-3804(12)60042-1.
- Lv, J., Jiang, F., Hu, T., Zhang, C., Huang, R., Hu, M., Xue, J., Huang, L., Wu, Y., 2023. Control of complex lithofacies on the shale oil potential in ancient alkaline lacustrine basins: the Fengcheng Formation, Mahu Sag, Junggar basin. Geoenergy Science and Engineering 224, 221501. https://doi.org/10.1016/ j.geoen.2023.211501.
- Loucks, R.G., Ruppel, S.C., 2007. Mississippian Barnett shale: lithofacies and depositional setting of a deepwater shale-gas succession in the Fort Worth Basin, Texas. AAPG (Am. Assoc. Pet. Geol.) Bull. 91 (4), 579–601. https://doi.org/10.1306/11020606059
- Mukhametdinova, A., Habina-Skrzyniarz, I., Kazak, A., Krzyzak, A.T., 2021. NMR relaxometry Interpretation of source rock liquid saturation-A Holistic approach. Mar. Petrol. Geol. 132, 105165. https://doi.org/10.1016/j.marpetgeo.2021.105165.
- Nelson, P.H., 2009. Pore-throat sizes in sandstones, tight sandstones, and shales. AAPG Bull. 93, 329–340. https://doi.org/10.1306/12141010019.
- Nie, H.K., Zhang, P.X., Bian, R.K., 2016. Oil accumulation characteristics of China continental shale. Earth Sci. Front. 23 (2), 55–62. https://doi.org/10.13745/ i.esf.2016.02.007.
- Pan, Y., Li, M., Sun, Y., Li, Z., Liao, L., Liao, Y., 2019. Characterization of free and bound bitumen fractions in a thermal maturation shale sequence. Part 1: acidic and neutral compounds by negative-ion ESI FT-ICR MS. Org. Geochem. 134, 1–15. https://doi.org/10.1016/j.orggeochem.2023.104640.
- Salama, A.M., Abd-Allah, Z.M., El-Sayed, M.I., Elbastawesy, M.A., 2021. Source rock evaluation and burial history modeling of Cretaceous rocks at the Khalda Concession of Abu Gharadig basin, western Desert, Egypt. J. Afr. Earth Sci. 184, 104372. https://doi.org/10.1016/j.jafrearsci.2021.104372.
- Shao, X., Pang, X., Li, H., Hu, T., Xu, T., Xu, Y., Li, B., 2018. Pore network characteristics of lacustrine shales in the Dongpu Depression, Bohai Bay Basin, China, with implications for oil retention. Mar. Petrol. Geol. 96, 457–473. https://doi.org/ 10.1016/j.marpetgeo.2018.06.015.
- Siddiqui, M.A.Q., Ali, S., Fei, H., Roshan, H., 2018. Current understanding of shale wettability: a review on contact angle measurements. Earth Sci. Rev. 181, 1–11.

- https://doi.org/10.1016/j.earscirev.2018.04.002.
- Tang, Y., He, W., Bai, Y., Zhang, X., Wu, W., 2021. Source rock evaluation and hydrocarbon generation model of a Permian alkaline lakes a case study of the Fengcheng Formation in the Mahu Sag, Junggar basin. Minerals 11 (6), 644. https://doi.org/10.3390/min11060644.
- Tao, K., Cao, J., Wang, Y., Ma, W., Xiang, B., Ren, J., Zhou, N., 2016. Geochemistry and origin of natural gas in the petroliferous Mahu sag, northwestern Junggar Basin, NW China: Carboniferous marine and Permian lacustrine gas systems. Org. Geochem. 100, 62–79. https://doi.org/10.1016/j.orggeochem.2016.08.004.
- Tao, K., Chen, X., Nueraili, Z.M., Hu, W., Shi, C., 2019. Deep hydrocarbons in the northwestern Junggar basin (NW China): geochemistry, origin, and implications for the oil vs. gas generation potential of post-mature saline lacustrine source rocks. Mar. Petrol. Geol. 109, 623–640. https://doi.org/10.1016/ j.marpetgeo.2019.06.041.
- Wang, E., Guo, T., Li, M., Xiong, L., Dong, X., Wang, T., Ouyang, J., 2023. Reservoir characteristics and oil properties of a lacustrine shale system: early Jurassic black shale from the Sichuan Basin, SW China. J. Asian Earth Sci. 242, 105491. https://doi.org/10.1016/j.jseaes.2022.105491.
- Wang, M., Li, M., Li, J., Xu, L., Zhang, J., 2022. The key parameter of shale oil resource evaluation: oil content. Petrol. Sci. 19 (4), 1443–1459. https://doi.org/10.1016/ i.petsci.2022.03.006.
- Wang, M., Ma, R., Li, J., Lu, S., Li, C., Guo, Z., Li, Z., 2019. Occurrence mechanism of lacustrine shale oil in the Paleogene Shahejie Formation of Jiyang depression, Bohai Bay Basin, China. Pet. Explor. Dev. 46 (4), 789–802. https://doi.org/ 10.1016/51876-3804/19)60242-9.
- Wu, Y., Liu, C., Jiang, F., Hu, T., Awan, R.S., Chen, Z., Lv, J., Zhang, C., Hu, M., Huang, R., Wu, G., 2022. Occurrence space and state of petroleum in lacustrine shale: insights from two-step pyrolysis and the N2 adsorption experiment. Energy & Fuels 36 (18), 10920–10933. https://doi.org/10.1021/acs.energyfuels.2c02222.
- Fuels 36 (18), 10920—10933. https://doi.org/10.1021/acs.energyfuels.2c02222. Xi, K., Zhang, Y., Cao, Y., Gong, J., Li, K., Lin, M., 2023. Control of micro-wettability of pore-throat on shale oil occurrence: a case study of laminated shale of Permian Lucaogou Formation in Jimusar Sag, Junggar Basin, NW China. Pet. Explor. Dev. 50 (2), 334—345. https://doi.org/10.1016/S1876-3804(23)60391-X.
- Xu, Y., Lun, Z., Pan, Z., Wang, H., Zhou, X., Zhao, C., Zhang, D., 2022. Occurrence space and state of shale oil: a review. J. Petrol. Sci. Eng. 211, 110183. https://doi.org/ 10.1016/j.petrol.2022.110183.
- Yu, K., Cao, Y., Qiu, L., Sun, P., 2019. Depositional environments in an arid, closed basin and their implications for oil and gas exploration: the lower Permian Fengcheng Formation in the Junggar Basin, China. AAPG Bull. 103 (9), 2073–2115. https://doi.org/10.1306/01301917414.
- Yu, K., Cao, Y., Qiu, L., Sun, P., Jia, X., Wan, M., 2018. Geochemical characteristics and origin of sodium carbonates in a closed alkaline basin: the lower Permian Fengcheng Formation in the Mahu sag, northwestern Junggar Basin, China. Palaeogeogr. Palaeoclimatol. Palaeoecol. 511, 506–531. https://doi.org/10.1016/ j.palaeo.2018.09.015.
- Zhang, C., Jiang, F., Hu, T., Chen, D., Huang, L., Jiang, Z., Wang, X., Liu, Z., Wu, Y., Lv, J., Huang, R., Hu, M., Wu, G., 2023. Oil occurrence state and quantity in alkaline lacustrine shale using a high-frequency NMR technique. Mar. Petrol. Geol. 154, 106302. https://doi.org/10.1016/j.marpetgeo.2023.106302.
- Zhang, L., Bao, Y., Li, J., Li, Z., Zhang, R., Zhang, J., 2014. Movability of lacustrine shaleoil: a case study of Dongying sag, Jiyang depression, Bohai Bay Basin. Pet. Explor. Dev. 41, 703–711. https://doi.org/10.1016/S1876-3804(14)60084-7.
- Zhang, P., Misch, D.M., Hu, F., Kostoglou, N., Sachsenhofer, R.F., Liu, Z., Meng, Q., Bechtel, A., 2021. Porosity evolution in organic matter-rich shales (Qingshankou Fm.; Songliao Basin, NE China): implications for shale oil retention. Mar. Petrol. Geol. 130, 105139. https://doi.org/10.1016/j.marpetgeo.2021.105139.
- Zhao, W., Hu, S., Hou, L., Yang, T., Li, X., Guo, B., Yang, Z., 2020. Types and resource potential of continental shale oil in China and its boundary with tight oil. Pet. Explor. Dev. 47, 1–11. https://doi.org/10.1016/S1876-3804(20)60001-5.
- Zhao, W., Bian, C., Li, Y., Zhang, J., He, K., Liu, W., Zhang, B., Lei, Z., Liu, C., Zhang, J., Guan, M., Liu, S., 2023. Enrichment factors of movable hydrocarbons in lacustrine shale oil and exploration potential of shale oil in Gulong Sag, Songliao Basin, NE China. Pet. Explor. Dev. 50 (3), 455–467. https://doi.org/10.1016/51876-3804(23)60407-0.
- Zhi, D., Tang, Y., He, W., Guo, X., Zheng, M., Huang, L., 2021. Orderly coexistence and accumulation models of conventional and unconventional hydrocarbons in lower Permian Fengcheng Formation, Mahu sag, Junggar Basin. Pet. Explor. Dev. 48, 43–59. https://doi.org/10.1016/S1876-3804(21)60004-6.
- Zhu, X., Cai, J., Liu, Q., Li, Z., Zhang, X., 2019. Thresholds of petroleum content and pore diameter for petroleum mobility in shale. AAPG (Am. Assoc. Pet. Geol.) Bull. 103 (3), 605–617. https://doi.org/10.1306/0816181617517009.
- Zou, C., Pan, S., Horsfield, B., Yang, Z., Zhang, L., 2019a. Oil retention and intrasource migration in the organic-rich lacustrine Chang 7 shale of the upper Triassic Yanchang Formation, Ordos Basin, central China. AAPG (Am. Assoc. Pet. Geol.) Bull. 103 (11), 2627–2663. https://doi.org/10.1306/01301917052.
- Zou, C., Zhu, R., Chen, Z., Ogg, J.G., Wu, S., Dong, D., Qiu, Z., Wang, Y., Wang, L., Lin, S., Cui, J., Su, L., Yang, Z., 2019b. Organic-matter-rich shales of China. Earth Sci. Rev. 189, 51–78. https://doi.org/10.1016/j.earscirev.2018.12.002.